SELF-ASSEMBLY AND DESIGN OF TUNABLE SOFT MATERIALS

RONALD J. PANDOLFI

A dissertation submitted to the Department of Physics in partial fulfillment of the requirements for the degree of Doctor of Philosophy

University of California, Merced
Nov 2014 – version 1.0.1

Defense committee:
Professor Jay E. Sharping, Chair
Professor Linda S. Hirst
Professor Michael E. Colvin
Professor Michael Scheibner

Ronald J. Pandolfi: *Self-assembly and Design of Tunable Soft Materials,* A dissertation submitted to the Department of Physics in partial fulfillment of the requirements for the degree of Doctor of Philosophy, © Nov 2014

The dissertation of Ronald J Pandolfi is approved, and it is acceptable in quality and form for publication on microfilm and electronically:

Professor Linda S. Hirst	Date
Professor Michael E. Colvin	Date
Professor Michael Scheibner	Date
Professor Jay E. Sharping, Chair	Date

University of California, Merced

2014

To Ayaka.

You are the perfect partner and friend. Thank you for your love and support.

To Mom and Dad.

You shared your enthusiasm for learning with me. Thank you for your inspiration and motivation.

To Unc L and Aunt C.

You are there when I need you. Thank you for your guidance and wisdom.

To my advisor, Linda.

You are a model scholar I truly esteem. Thank you for your valuable time and insight.

To my colleagues.

We've shared long nights of fine work. Thank you for your cooperation and trust.

El Psy Congroo.

— Kyouma Hououin

ABSTRACT

Soft materials are a diverse and rich field of interest. Materials which form structure by their own self-assembly are of special interest. New material properties can be achieved by the self-assembly of constituent soft matter. Two soft matter systems are investigated in this dissertation from different perspectives. An *in silico* approach is applied to explore semiflexible polymers; X-ray scattering is applied to probe quantum dot (QD)-liquid crystal (LC) composites.

Semiflexible polymers can generate a range of filamentous networks significantly different in structure from those seen in conventional polymer solutions. Our coarse-grained simulations with an implicit cross-linker potential show that networks of branching bundles, knotted morphologies, and structural chirality can be generated by a generalized approach independent of specific cross-linkers. Network structure depends primarily on filament flexibility and separation, with significant connectivity increase after percolation. Results should guide the design of engineered semiflexible polymers.

Thermotropic liquid crystal provides an active basis for organization of nanoparticles. Using a bottom-up approach, nanoparticles well dispersed in the isotropic phase can be self-assembled by exclusion from the nematic phase as the material cools from the isotropic phase. A ligand exchange reaction can be used to create nanoparticles with mesogenic ligand coatings to allow better dispersion and assemble novel structures. Small angle X-ray scattering is used to inform the structure of a variety of materials which apply this design concept. These metamaterials have tunable properties with applications in quantum dot based electro-optic devices and more.

PUBLICATIONS

Some ideas and figures have appeared previously in the following publications:

"Self-Assembled nanoparticle micro-shells templated by liquid crystal sorting"
A. Rodarte, B. Cao, H. Panesar, R. J. Pandolfi, M. Quint, L. Edwards, S. Ghosh, J. Hein, L. S. Hirst, Soft Matter, in press (2014).

"Magnetic field induced brightening in liquid crystal synergized magnetic and semiconducting nanoparticle composite assemblies"
J. Amaral, J. Wan, A. Rodarte, M. Quint, R. J. Pandolfi, M. Scheibner, L. S. Hirst, S. Ghosh, Soft Matter, DOI: 10.1039/C4SM02015D (2014). (Available online)

"An analytic toolbox for simulated filament networks"
R. J. Pandolfi, L. Edwards, L. S. Hirst, Mrss14-1688-y05-18 Spring 2014 MRS proceedings (2014). (Available online)

"Designing highly tunable semi-flexible filament networks"
R. J. Pandolfi, L. Edwards, D. Johnston, P. Becich, and L. S. Hirst, Phys. Rev. E , 89(6):062602, June (2014). (Available online)

"Tuning quantum dot organization in liquid crystal for robust photonics applications"
A. L. Rodarte, Z. S. Nuno, B. H. Cao, R. J. Pandolfi, M. T. Quint, S. Ghosh, J. E. Hein, and L. S. Hirst, CHEM PHYS CHEM, Volume 15, Issue 7, pages 1413–1421, (2014). (Available online)

"Quantum dot/liquid crystal composite materials: Self-assembly driven by liquid crystal phase transition templating"
A. L. Rodarte, R. J. Pandolfi, S. Ghosh, and L. S. Hirst, J. Mater. Chem. C 1, 5527 (2013). (Available online)

ACKNOWLEDGMENTS

I would like to thank the UC Merced Physics faculty, most importantly my advisor Linda S. Hirst who has positively influenced my career and life. She is a brilliant mentor who has taught me more than Physics, diligence, and leadership. I have built confidence and friendships in the group she created. I will always consider her my mentor and myself a member of the Hirst Group.

The other Physics faculty have also been supportive through my studies. The collaborations with Jason Hein, Sayantani Ghosh, and their students have been essential to much of my studies. Together with Linda these three form an impressive team; I wish great success for their future.

The lab members have also supported me through collaborations and general assistance. Lauren Edwards, David Johnston, Peter Becich, and Ashley Ahrens-Braunstein made valuable contributions to the goals of this dissertation. Special thanks to friends Andrea Rodarte, Jussi Amaral, Makiko Quint, and Zachary Nuno for including me in their projects. Chai Lor, Pradeep Uppamoochikkal, and Nathan Melton have been great friends who provided valuable advice and support.

Special access to a 3D printer was made available by YangQuan Chen, Brandon Stark, and the MESA Lab. The knowledge and resources they shared were essential to completing the magnetic sample stage for small angle X-ray scattering (SAXS) experiments.

I acknowledge support via internal funding from the UC Merced graduate group. The Physics group has been very helpful in coordinating financial assistance; thanks to Physics chairs Ajay Gopinathan, Linda Hirst, Jay Sharping, and Sayantani Ghosh.

Thank you everyone for your kind encouragement and assistance.

RONALD J PANDOLFI | CURRICULUM VITAE

CONTACT

1091 W Yosemite Ave Apt 3 Merced CA, 95348
E-mail: ronpandolfi@gmail.com
Phone: 703.615.6738

EDUCATION

Ph.D. in Physics

Fall 2009 — Dec 2014
University of California, Merced
Specialty: Molecular dynamics simulation, soft matter x-ray diffraction
Advisor: Prof. Linda S. Hirst

B.S. in Physics, Mathematics

Fall 2005 — Spring 2009
Randolph-Macon College

PAPERS

"Self-Assembled nanoparticle micro-shells templated by liquid crystal sorting"
A. Rodarte, B. Cao, H. Panesar, R. J. Pandolfi, M. Quint, L. Edwards, S. Ghosh, J. Hein, L. S. Hirst, Submitted (2014)

"Magnetic field induced brightening in liquid crystal synergized magnetic and semiconducting nanoparticle composite assemblies"
J. Amaral, J. Wan, A. Rodarte, M. Quint, R. J. Pandolfi, M. Scheibner, L. S. Hirst, S. Ghosh, Soft Matter, DOI: 10.1039/C4SM02015D (2014). (Available online)

"An analytic toolbox for simulated filament networks"
R. J. Pandolfi, L. Edwards, L. S. Hirst, Mrss14-1688-y05-18 Spring 2014 MRS proceedings (2014). (Available online)

"Designing highly tunable semi-flexible filament networks"
R. J. Pandolfi, L. Edwards, D. Johnston, P. Becich, and L. S. Hirst, Phys. Rev. E (2014). (Available online)

"Tuning quantum dot organization in liquid crystal for robust photonics applications"
A. L. Rodarte, Z. S. Nuno, B. H. Cao, R. J. Pandolfi, M. T. Quint, S. Ghosh, J. E. Hein, and L. S. Hirst, CHEM PHYS CHEM, Volume 15, Issue 7, pages 1413–1421, (2014). (Available online)

"Quantum dot/liquid crystal composite materials: Self-assembly driven by liquid crystal phase transition templating"
A. L. Rodarte, R. J. Pandolfi, S. Ghosh, and L. S. Hirst, J. Mater. Chem. C 1, 5527 (2013). (Available online)

PRESENTATIONS

An Analytic Toolbox for Simulated Networks, Poster, R. J. Pandolfi, L. Edwards, L. S. Hirst, Materials Research Society, Apr 2014.

Designing Highly Tunable Semiflexible Filament Networks, Poster, R. J. Pandolfi, L. Edwards, L. S. Hirst, Biophysical Society Meeting, Feb 2014.

Designing Highly Filament Networks, R. J. Pandolfi, L. Edwards, L. S. Hirst, APS CA-NV Regional Conference, Nov 2013.

Actin Network Molecular Dynamics Simulation with Filamin and α-actinin, Poster, R. J. Pandolfi, L. Edwards, D. Johnston, P. Becich, L. S. Hirst, University of California, Merced, Student Research Poster Competition, April 2012 – Nat. Sci. Undergraduate Prize Winner.

Actin Network Molecular Dynamics Simulation with Filamin and α-actinin, Poster, R. J. Pandolfi, L. Edwards, D. Johnston, P. Becich, L. S. Hirst, Biophysical Society Meeting, February 2012.

Molecular Dynamics Modeling of Actin Network Formation, R. J. Pandolfi, P. Becich, L. Nguyen, and L. S. Hirst, APS March Meeting 2011.

Molecular Dynamics Modeling and Analysis of Actin Network Formation, R. J. Pandolfi, L. S. Hirst, L. T. Nguyen, P. Becich, A. Ahrens, L. Edwards, and D. Johnston, APS CA-NV Regional Conference, Nov 2011.

Molecular Dynamics Simulation of Actin Network Formation, Poster, University of California, Merced, Student Research Poster Competition, April 2011 – Nat. Sci. Graduate Prize Winner.

WORK EXPERIENCE

University of California, Merced, Summer 2010 — Present

Graduate Student Researcher
Investigated semi-flexible filament network formation by molecular dynamics simulation

- Developed molecular dynamics software, models, and experimental methods
- Synchrotron beamline automation apparatus design with 3D printing
- Lead experimenter for Stanford Synchrotron Radiation Lightsource beamline run for group projects

University of California, Merced, Fall 2009 — Present

Teaching Assistant

- Teaching, grading, and proctoring in both discussion sessions and lab sessions
- Hours worked per week: 20 hours

Stanford Synchrotron Radiation Lightsource, SLAC National Accelerator Laboratory, May 2009 — Aug 2009

Summer Undergraduate Laboratory Internship

- Second internship awarded through SULI program
- Developed and implemented a system for crystallographic texture analysis for use with Stanford Synchrotron Radiation Lightsource beamline 11-3
- Ran beam-line hutch experiment to obtain test data
- Cooperated in monitoring group's beam-line experiments in shifts

Thomas Jefferson National Accelerator Facility, May 2009 — Aug 2009

Summer Undergraduate Laboratory Internship

- Internship acquired through the SULI program
- Conducted analysis of data from measurements on nucleon spin structure at low Q^2 (Jlab E97-110)

Randolph-Macon College, Marketing and Communications Department, Sep 2005 — May 2009

Web Assistant

- Provide assistance to faculty and staff with web development tasks, with emphasis on web programming
- Assist in site administration and development of the school site
- Aided in a successful full site redesign and CMS implementation
- Hours worked per week: 8 Hours

National Science Resources Center - Communications and Media division, May 2006 — Aug 2006

Intern

- Assisted in web-development and programming
- Helped develop science education materials including additions to the Science and Technology Concepts series and materials for the 2007 Smithsonian Science Education Academies for Teachers

MITRE Corporation, McLean, VA, May 2004 — July 2004

Technical Summer Intern

SPECIALIZED SKILLS

Proficiency in:

- C, C++

- Python
- Matlab
- Mathematica
- LaTeX
- ASP.NET, VB .NET, C# .NET
- SQL
- Web languages: HTML, CSS, JavaScript, XML
- Linux (prefer Arch, #!, Ubuntu)
- Graphics editing software
- Solidworks

CONTENTS

LIST OF FIGURES

LIST OF TABLES

ACRONYMS

GPU graphics processing unit

LC liquid crystal

QD quantum dot

5CB 4-Cyano-4′-pentylbiphenyl

SAXS small angle X-ray scattering

NP nanoparticle

MNP magnetic nanoparticles

MOKE magneto-optic Kerr effect

PL photoluminescence

ODA octadecylamine

TEM transmission electron microscope

SSRL Stanford Synchrotron Radiation Lightsource

PLA polylactic acid

SSH secure shell

DISSERTATION OVERVIEW

DISSERTATION ORGANIZATION

This dissertation is organized in two parts. For the project discussed in the first part, "Designing Semiflexible Polymer Networks," I was the only graduate student contributing to the project. The project discussed in the second part, "Quantum Dot/Liquid Crystal Self-assembly," is a collaboration across the research groups of Profs. Linda S. Hirst, Sayantani Ghosh, and Jason Hein. The nature of the project requires a multi-disciplinary coordination of these soft matter physics, optics, and chemistry groups. Many graduate students have been involved in this project. My research involvements in these two parts are presented in my dissertation; the work presented in the second part focuses on my contributions.

While these two parts seem disparate, I see both as attractive topics for research. I have also used the opportunity to work on both as a way of extending my skill set in preparation for post-graduate career. I have had the freedom to build experience in different directions including: molecular dynamics, scientific programming, x-ray diffraction experiments, and apparatus engineering/design.

Part I

DESIGNING SEMIFLEXIBLE POLYMER NETWORKS

Semiflexible polymers can generate a range of filamentous networks significantly different in structure from those seen in conventional polymer solutions. Our coarse-grained simulations with an implicit cross-linker potential show that networks of branching bundles, knotted morphologies, and structural chirality can be generated by a generalized approach independent of specific crosslinkers. Network structure depends primarily on filament flexibility and separation, with significant connectivity increase after percolation. Results should guide the design of engineered semiflexible polymers.

1 INTRODUCTION

1.1 INTRODUCTION

1.1.1 *Semi-Flexible Polymer Networks*

In biology semi-flexible polymers are common. For example, F-actin filaments, microtubules and intermediate filaments form the cellular cytoskeleton, cross-linking via the action of a variety of different associated proteins [5]. Recent experimental work has explored the generation of synthetic, peptide based filaments [6], however semi-flexible polymers have been little explored for practical materials applications despite their potential to produce unique structures [7–9], light yet rigid gels [10], materials for mesoscale templating [9], biological scaffolds for tissue engineering [11], and drug delivery [12–14].

Semi-flexible polymers have the potential to generate a diverse family of network-based materials. Such materials differ significantly in structure from those seen in polymeric systems formed from molecules approximated by the freely jointed chain. The solution behavior is well known for specific biological examples such as F-actin, microtubules, DNA etc. under the influence of cross-linking proteins or specific ionic conditions. However, a general picture of phase behavior and the range of accessible structures as a function of flexibility, length, attractive potential, and concentration has not yet emerged as these parameters are often difficult to tune experimentally. The general principles for assembly and structure tuning we demonstrate open the field for the generation of a wide range of new materials, incorporating semiflexible filaments as the basic unit. There has been limited work dedicated to the formation of materials from stiffer polymers (micron scale persistence length) since most widely used polymer chains are highly flexible. This area of interest has grown recently with a large number of experimental and theoretical studies on the behavior of semiflexible filaments in solution, most biological in origin (i.e. F-actin, DNA etc) [7, 8, 15–33]. Recently Kouwer et al. experimentally demonstrated network formation from a polyisocyanopeptide fiber hydrogel with tunable mechanical properties [6]. These materials provide a basis to experimentally investigate functional biomimetic synthetic hydrogels and their applications.

In this dissertation we explore the range of structures accessible for a semi-flexible filament self-assembly. Our coarse-grained model, inspired by models of F-actin networks with explicit cross-linkers, greatly expands the accessible param-

eter space. Approximating the effect of crosslinkers allows for a more tunable representation of filament attraction and binding. Morphological properties of the networks are quantitatively examined using connectivity analysis, radial pair distribution functions and a scaling analysis. We demonstrate that hierarchical network structures such as the branching bundle network seen in biological [7, 15, 16] and synthetic [6] materials do not depend on specific cross-linker interactions, and that these structures can be generated by simple attractive potentials.

Our results reveal that previously observed networks of bundles seen in F-actin systems are not unique to certain cross-linkers but occupy a tunable position in the phase diagram, controlled primarily by filament flexibility and minimum coaxial distance. Filament length is found to have a lesser role, with a minimum length required for network formation. Further modification of filament parameters allows the generation of hierarchically structured networks not seen in flexible polymer systems, such as knotted networks, transverse bundle packing and examples of structural chirality. Detailing the effects of semi-flexible filament parameters on structure and connectivity in this way provides a roadmap for the design of highly tunable hierarchical networks and aids in the discovery of previously unseen structures for novel bioinspired materials.

1.2 BACKGROUND

1.2.1 *Semiflexible Polymer Filaments*

A polymer is an arrangement of subunit molecules bound to each other in series. Polymers may be formed from synthetic monomers such as polystyrene, though they are also formed as essential components of biological systems. Polymers are ubituitous in materials science, though semiflexible polymers are a much more specialized area of study. Semiflexible polymers are critical in biological systems, in which they naturally form to serve as structural components and other cellular functions.

1.2.1.1 *Biological Context*

Biopolymers include polynucleotides, polypeptides, and polysaccharides. The structural conformation of many biopolymers can be approximated by an ideal or freely-jointed chain reminiscent of a 3D random walk. However, a select group of biopolymers instead form more rigid structures between the limits of flexibility. More flexibile than a rigid rod, but less flexible than a freely-jointed chain, *semiflexible* biopolymers such as F-actin and microtubles are critical to cellular function and form part of the cytoskeleton. Semiflexible polymers have persistence lengths on the order of their contour lengths. The biopolymer F-actin is an excellent ex-

ample material from which the broader subject may be discussed due to having been well investigated in previous works.

In a biological context, F-actin forms an important part of the cytoskeleton by connecting with other Actin filaments via crosslinking proteins. By crosslinking together, more complex structures form from individual filaments. Filaments may bundle together and/or form a network structure by making connections with nearby filaments (see Figure 1). A diverse group of crosslinkers exist for F-actin. While some such as Filamin may induce additional geometry due to their inherent binding configuration, a wider group simply form point-to-point bindings of various distances between filaments, such as Fascin, Fimbrin, α-actinin, and Spectrin. F-actin and similar materials are able to form a vast array of structural morphologies by self-assembly with crosslinking proteins, however they limited in configuration by the inherent properties of the filament, most importantly flexibility. In order to develop new materials which are inspired by or mimic these biological systems, interest has built in developing synthetic semiflexible polymer filaments.

1.2.1.2 *Generalized Materials Design*

In contrast to natural biopolymers, synthetic semiflexible polymers can have tunable properties. Kouwer et al. demonstrated synthesis of peptide based semiflexible polymers with tunable persistence length which can also mimic biopolymers[6]. A broader understanding of the effects of synthetic materials such as these may be tuned to produce structural morphologies as desired for application.

1.2.2 *Molecular Dynamics*

Molecular dynamics (MD) is a style of computer simulation of the physical interactions and movement of particles. This is typically applied based on an atomistic approach with every atom individually represented as point particles. Coarse-graining simplifications to atomistic models are common. The structure of the object to be simulated (i.e. a DNA segment) is defined with the masses, charges, and bonds of each unit. From some initial positional condition, the process of molecular dynamics evolves the simulation by projecting trajectories of each element based on potential energy functions defining interactive forces between elements.

A robust integration method used to compute trajectories in molecular dynamics is the *velocity Verlet* scheme. By this method, for each following step $(t + \Delta t)$, the new position, velocity, and acceleration for each particle are calculated from the previous values:

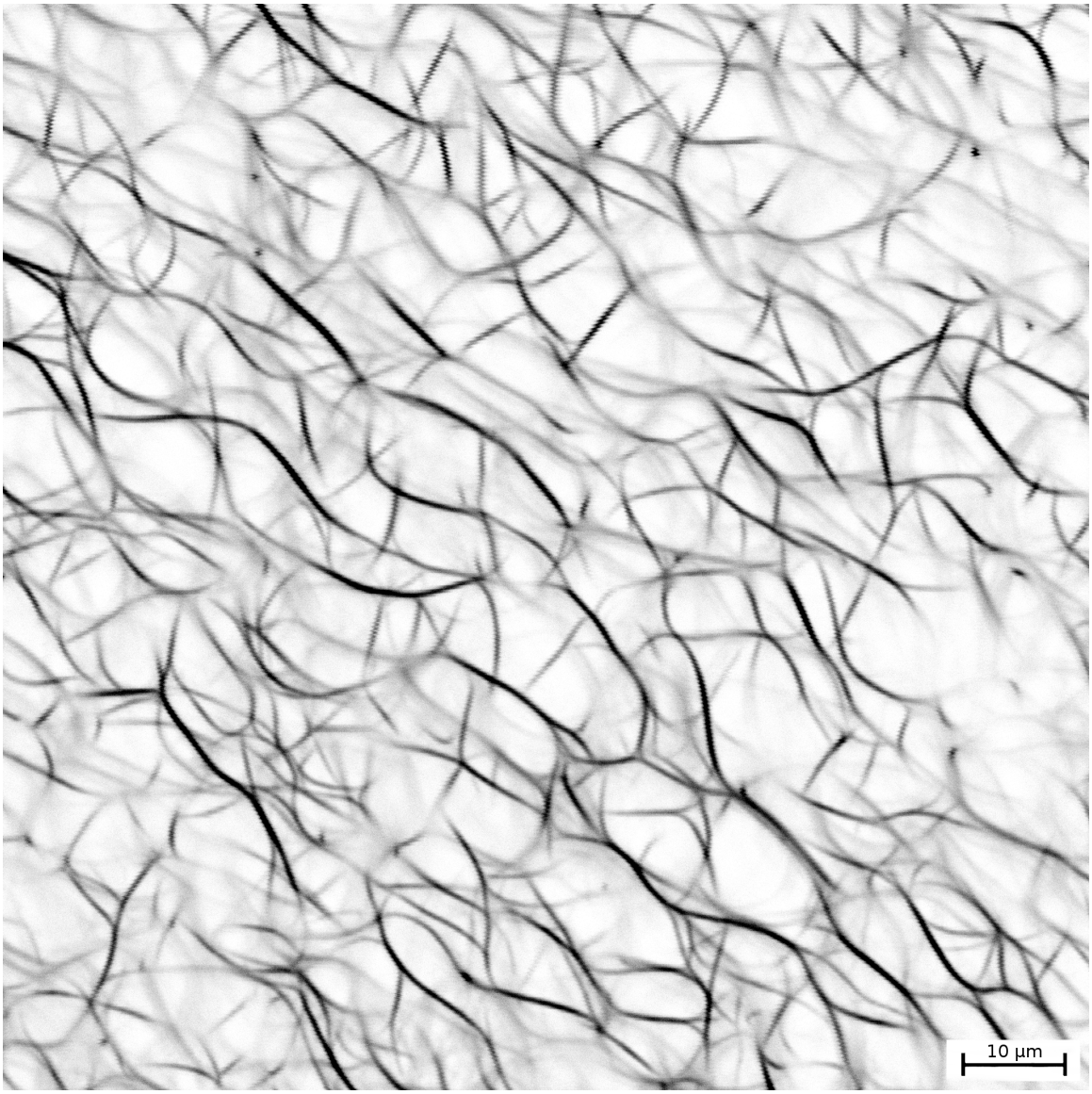

Figure 1: A maximum-intensity projection of a confocal microscopy image z-stack showing the branching bundle network structure of F-actin at 0.015 mg/ml, with α-actinin at a 5:1 ratio with the G-actin monomer, inverted. Alexa Fluor 488 Phalloidin binds with the F-actin filaments at a ratio of 1:1 with the monomer, providing the fluorescence contrast.

$$\vec{r}\,(t+\Delta t) = \vec{r}(t) + \vec{v}(t)\Delta t + \frac{1}{2}\vec{a}(t)\Delta t^2$$

$$\vec{v}\left(t+\frac{1}{2}\Delta t\right) = \vec{v}(t) + \frac{1}{2}\vec{a}(t)\Delta t$$

$$\vec{a}\,(t+\Delta t) = -\frac{\nabla V\left(\vec{r}\,(t+\Delta t)\right)}{m}$$

$$\vec{v}\,(t+\Delta t) = \vec{v}\left(t+\frac{1}{2}\Delta t\right) + \frac{1}{2}\vec{a}\,(t+\Delta t)\,\Delta t$$

for mass m, position $\vec{r}(t)$, velocity $\vec{v}(t)$, acceleration $\vec{a}(t)$, potential $V(\vec{r})$, and timestep Δt. This integration method has numerical and computational advantages over other methods such as the simpler *Verlet* method. The software used for MD simulations in this dissertation, NAMD, applies this method.

An energy minimization procedure is typically applied to the initial state of a molecule in order to correct poor placement, such as bad contacts between atoms. This procedure aims only to find a localized energy minimum, removing excess potential energy based on positional conformation.

In atomistic-scale MD simulations, the role of solvent interactions are emphatically important. A variety of explicit and implicit solvent models have been developed for this purpose in MD simulation software. In contrast, the simulations presented in this dissertation have a coarse-grained minimum spacing of ~10 nm, far greater than typical MD systems. On this scale, hydrophic effects and electrostatic screening resulting from water solvation are diminished. Conveniently, Langevin dynamics is then well suited to this regime, as it neglects those effects but models the viscosity of a solvent and controls the temperature of the system. A dissipative and fluctuating force term are added to effectively model the system's coupling to the solvent reservoir:

$$m\vec{a} = -\nabla V - \gamma\vec{v} - \sqrt{\frac{2\gamma k_B T}{m}}\vec{R}(t)$$

for temperature T, Boltzmann constant k_B, univariate random Gaussian process $\vec{R}(t)$, and friction coefficient γ. The MD software NAMD implements this by modifying the velocity Verlet integration scheme to use the Brünger-Brooks-Karplus (BBK) method [34].

1.2.2.1 *Hardware for MD simulations*

For large simulations, a massive number of calculations are computed for each timestep. Hardware with significant computational power is typically required for a reasonable completion duration. Modern solutions to this involve parallel

computation of mathematical operations, with a few options for approach. Multi-core processing, networked multi-processor computing, and graphics processing unit (GPU) computing may be utilized separately or all at once with scalable software such as NAMD to improve computation time by orders of magnitude.

2

METHODS

This chapter discusses the methods used to model, simulate, and characterize semiflexible polymer filament systems.

2.1 MOLECULAR DYNAMICS MODELS

2.1.1 *Semiflexible Polymer Filament Model*

Filaments are modeled as a bead-spring chain. With the distance between beads as a tunable quantity, the mass of each bead is set equal to the mass of a same-length F-actin segment based on the mass per unit length of F-actin.

The semiflexibility of filaments is modeled by the Euler angle θ for any 3-bead segment (see Figure 2) with an energy cost described by:

$$V = \sum_{angles} k_\theta \left(\theta - \theta_0\right)^2$$

$$k_\theta = \frac{L_P}{\Delta L} k_B T$$

$$\langle \cos\theta \rangle = e^{-\Delta L / L_P}$$

with bead-bead spacing ΔL, persistence length L_P, and relaxation angle $\theta_0 = 180°$. The relationship with L_P allows definition of filament flexibility based on measured values of persistence length for individual filaments.

A spring potential is applied to every 2-bead segment, providing the filament structure by:

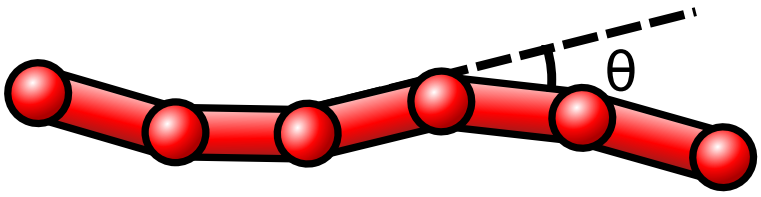

Figure 2: Semiflexible filament model diagram. Circles represent point mass beads; they are joined by massless rods. An Euler angle θ is labeled.

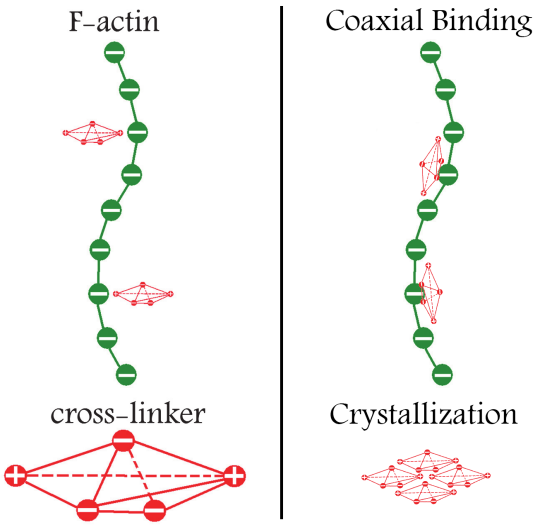

Figure 3: Discrete crosslinker model (left) and artifacts of this model (right)

$$V = \sum_{bonds} k_b(b - b_0)^2$$

where $b - b_0$ is the difference from equilibrium distance, and k_b is the spring constant. The coefficient k_b is large, as an approximation of a non-stretching filament.

The 1-4 exclusion setting in NAMD is used to exclude intra-filament force calculations for same-filament beads which are nearly adjacent (within 3 bond links).

2.1.2 *Discrete Crosslinker Model*

The discrete crosslinker approach models crosslinkers as polyhedra of static charges such that the ends are attracted to bind with filaments (see Figure 3, left). The discrete crosslinker model approach was applied successfully to simulating a polymer network system [22, 23], and investigating the role of F-actin:α-actinin molar ratio in network structure. However in some cases unfavorable results are produced as artifacts of the model. Artifacts of this approach include: same-filament binding and localized crystallization (see Figure 3, right). Additional residue-based course-graining is required with this approach, representing many crosslinkers as one polyhedra. This approach is also computationally more costly, as there are many more residues in a simulation with their addition.

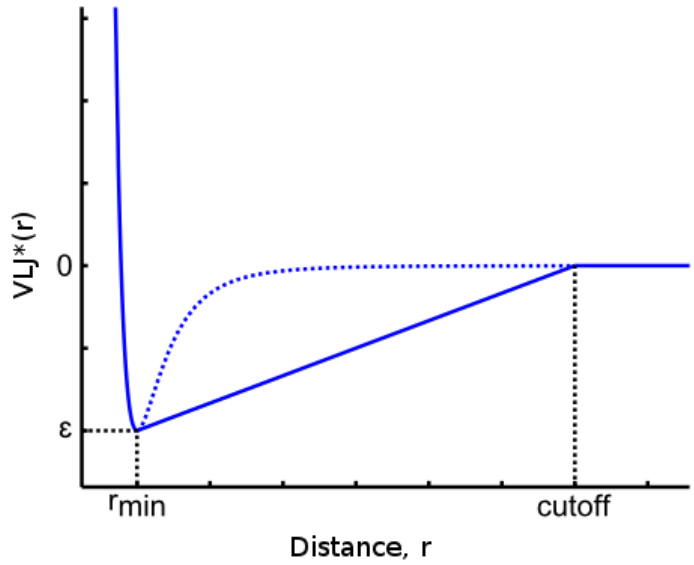

Figure 4: Lennard Jones Potential (dashed) with a linear long range potential.

2.1.3 *Potential Field Crosslinker Model*

An alternative approach to the discrete crosslinker model is a mean-field-like approach by which discrete crosslinkers are replaced by an inter-filament potential. This potential model describes the minimum spacing (length) of a crosslinker and the long range affinity to bind.

A modified Lennard-Jones potential V_{LJ*} with a linear regime is used to model the long-range attractive potential and minimum filament spacing of cross-linkers implicitly with as a piecewise function (see Figure 4).

$$V_{LJ*}(r) = \begin{cases} \varepsilon \left[\left(\frac{r_{min}}{r}\right)^{12} - 2\left(\frac{r_{min}}{r}\right)^{6} \right], & r < r_{min} \\ -\varepsilon \left[\frac{r_{min} - r}{cutoff - r_{min}} + 1 \right], & r \geq r_{min} \end{cases}$$

The base Lennard-Jones potential's long range behavior is highly dependent on r_{min}. The appended long-range linear regime allows for a more consistent attractive potential across different r_{min} with a cutoff distance of 440 nm limiting the range of attraction. The cutoff does not interrupt structure formation, as it is much larger than the average spacing between bundles in a network. This model allows parametrization of the binding energy/attraction strength ε and minimum coaxial distance r_{min}.

2.1.3.1 *Improving the potential function*

The piecewise substitution of a linear function as part of the potential is a minimalist solution to creating a more uniform long range attraction across different r_{min} values. This is simple to implement in NAMD by taking advantage of the switching function which is more commonly used for the smooth truncation of long range potentials. This potential is simple and effective, however some improvements may be made to model the force in a smoother way.

A smooth first derivative would be more natural. Such specialized potential functions would require modification of the NAMD source to implement.

2.1.4 *Hybrid Model*

The potential field crosslinker model is a more robust and tunable approach compared with the discrete crosslinker model, however it also has an artifact: parallel bound filaments may creep along eachother until their ends align. This effect is strongly dominant with bundles of short filaments, although it is likely present to a lesser extent in other regimes. The discrete crosslinker model also produces unfavorable localized crystallization and same-filament binding.

A proposed solution to eliminate these artifacts is to take a hybrid approach. By applying the potential field model along with a more sparse (coarse grained) distribution of discrete crosslinkers, both artifacts might be eliminated. The sparse dispersity of discrete crosslinkers would prevent localized crystallization. The discrete crosslinkers would also form site-to-site bonds which might be strong enough to prevent parallel filaments from creeping along eachother into adjacency, an artifact dominant with isolated bundles. The false scaled concentration of discrete crosslinkers would be balanced by the strength of the potential field model.

By combining these models, a mutualistic hybrid model may be achieved, further improving network simulation mechanics.

2.1.5 *Generating Simulation Files*

For a NAMD simulation, the files required to run a simulation are listed in Table 1.

The parameterized generation of these files was automated for the purpose of creating large arrays of simulations. A python script generates all of these files, and can by invoked by a shell or python script to generate simulation arrays. The program script accepts the non-positional arguments in Table 2.

This script also accepts a directory path which it will use as a root to populate.

*.inp	Minimization/production run procedure
*.inp	Potential function parameters (CHARMM format)
*.psf	Bonds (X-PLOR format)
*.pdb	Initial coordinates (CHARMM format)
*.inp (optional)	Bond structure (CHARMM format) for visualization or generating *.psf

Table 1: Components of a simulation in NAMD

-bb	bead-bead spacing along the same filament
-f	bending stiffness energy
-r	minimum coaxial distance, r_{min}
-eps	binding energy, potential strength
-fil	number of filaments
-beads	number of beads per filament
-t	number of timesteps
-box	box size (nm)
-cls	number of crosslinkers (set to zero for implicit model)
-g	gaussian chain generator (use for diagnostics)

Table 2: Simpop.py simulation files generator arguments

Processor	AMD Phenom II X6 1055T 2.8GHz Socket AM3 125W Six-Core Desktop Processor
Power Supply	RAIDMAX HYBRID 2 RX-630SS 630W ATX12V V2.2/EPS12V
RAM	G.SKILL Ripjaws Series 16GB (4 x 4GB) 240-Pin DDR3 SDRAM DDR3 1333 (PC3 10666)
Motherboard	MSI NF750-G55 ATX AMD Motherboard

Table 3: Hardware specifications for Karasu workstation

2.2 MOLECULAR DYNAMICS ENVIRONMENT

2.2.1 *Environment Model*

Batch simulations were completed in a periodic box with side length 3.23 µm. Larger simulations have been completed at up 6.46 and 9.69 µm.

A Langevin thermostat is applied with every integrator step. Langevin dynamics adds additional random forces and damping which models a solvent at a stable temperature. This approach does not qualify as a full implicit solvent model, as it lacks inclusion of electrostatic screening, hydrophobic effects, and hydrodynamic interactions. The exclusion of these effects is appropriate to this system, since they have limited influence in the mesoscale regime investigated.

A 5 ps timestep is used, with one frame being recorded every 50 timesteps.

2.2.2 *Hardware*

The Ranger Sun Constellation Linux computing cluster at University of Texas provided 200000 Service Units for this project through the XSEDE program, most of which was used. The time overhead of queuing a job on Ranger was a few days, making it prohibitively time-costly except for the longest simulations.

The Karasu (Komputation Accelerating Research and Simulation Unit) workstation was assembled as a local alternative optimized for CUDA GPU computing on a budget limited to $1000 (see Table 3 for specifications). This workstation has served as a programming, MD simulation, and Linux learning platform for five students.

The NVIDIA GTX 550 Ti card was selected in 2011 for our GPU computing simulation system. This processor had mixed popular opinions due to its lower performance in comparison to the earlier generation 400 series processors with higher memory bus bandwidth. The significantly lower price and power consumption of the 550 Ti over earlier generation cards made it a viable option for this system.

Since this decision is no longer relevant with newer generations of cards available, a general suggestion to optimize performance capability for CUDA simulations is to optimize memory bus bandwidth, CUDA Compute capability, and processor clock speed. Crypto-currency hashing GPU benchmarks now provide a unified metric for predicting performance for simulations.

2.2.3 *Software and Utilities*

The Ubuntu 10.04 LTS and 12.04 LTS Linux distributions were used as operating systems for the Karasu workstation. The Linux CUDA toolkit and driver were installed to allow GPU optimized applications access to the graphics card. The networked resource monitoring tool Munin was used to observe and analyze resource trends and performance issues. This tool is specially helpful for checking system load remotely, such as when waiting for a process to finish or checking load before starting a resource intensive process. Munin statistics can be viewed at:

`http://karasu.ronpandolfi.com/munin/`

The molecular dynamics software NAMD was used for simulations. This simulation platform is highly scalable and has GPU optimization. It also integrates well with the popular MD visualization tool VMD, and is compatible with CHARMM format files.

2.3 SELECTION OF ε

The bond strength parameterized in the modified LJ potential function was originally modelled from the bond strength of α-actinin. The phase space across ε, $r_{\min}$, and L_P was investigated in order to check the richness of the phase space as it depends on the strength of the attractive potential. A fixed filament length of 1 µm was used in this portion of the study to anchor the scale of the simulation. At a lower limit, small ε reduces the rate of network formation, limiting the growth of structure and favoring low-complexity structures. At an upper limit, large ε affects the accuracy of the integrator, requiring shorter timesteps and favoring high-complexity structures. In order to select a value which would present a rich phase space, an array of simulations across varied ε, $r_{\min}$, and L_P was first analyzed. The most complex and well behaved phase space was found to occur at $\varepsilon = -0.061$ cal/mol.

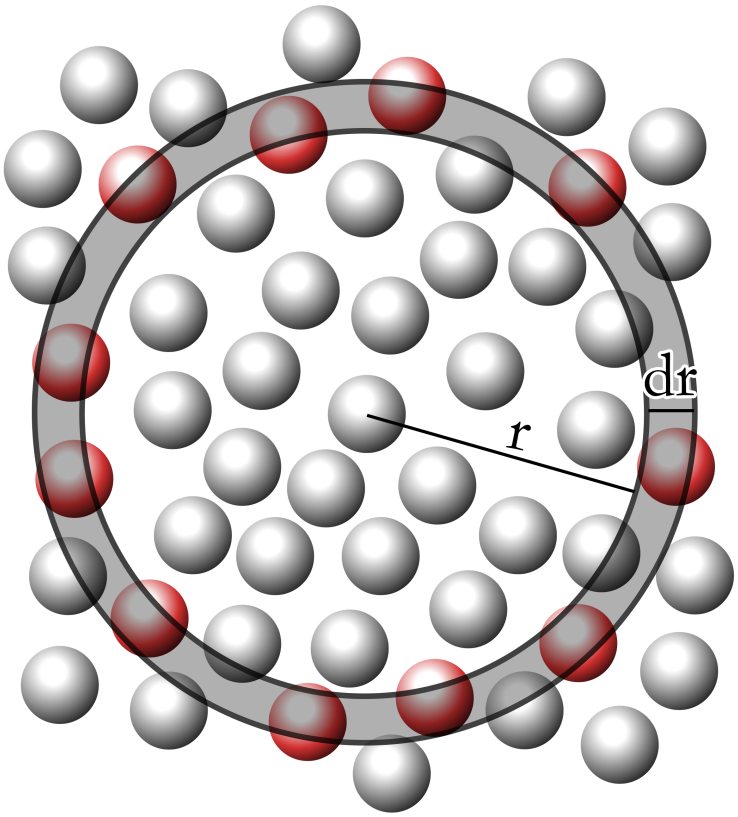

Figure 5: Diagram of RDF calculation for a single source bead. The scaled density is calculated at each radius r for spherical shells of width dr.

2.4 RADIAL DISTRIBUTION FUNCTION

The Radial-pair Distribution Function (RDF) is a staple analytical technique [35] in Molecular Dynamics that describes the mass-density at various length scales as a radially symmetric probability density function (see Figure 5). Applied to a simulated network, this is useful for identifying filament packing structure (i.e. filament arrangement within a bundle), bundle thickness, and network mesh size.

The RDF, $G(r)$, is calculated as a summation over every bead k for N beads in volume V, with bin size dr and $n(r)$ beads in the spherical shell of width dr and radius r centered at k:

$$g_k(r) = \frac{n(r)}{4\pi r^2 dr}\left(\frac{V}{N}\right)$$

$$G(r) = \frac{1}{N}\sum_{k=1}^{N} g_k(r)$$

A few cautions are important when applying this to a simulated network. The bead-bead spacing along a filament is a highly ordered structure that would leave an artifact in the RDF. To eliminate this, spline interpolation can be used to the extent that the interpolated bead-bead spacing is equal the spatial resolution of the RDF. In the calculation of $g_k(r)$ for some bead k, beads on the same filament as k can be excluded from the $g_k(r)$ to remove the signature of a filament's average contour from the final RDF. This provides a clearer representation of the network structure. The spatial periodicity of the system must also be accounted for when determining the distance between beads. The nearest of the nearest-neighbor images must be used.

Computational cost for these calculations scales with N^2, and spline interpolation effectively increases N significantly, further increasing cost. To improve efficiency, GPU parallel processing is suggested to decrease computation time. Undersampling can also be applied for more cursory computation.

2.5 FRACTAL DIMENSION

The fractal dimension (or 'mass-density power-law scaling') of a structure represents the way mass scales with space. Common simple geometries have fractal dimension values which serve as a good reference when looking at more complex structures. For example, a straight line (i.e. a single filament) in 3D has a fractal dimension of $D = 1$. A plane, $D = 2$ (i.e. a thin sheet of material) and a volume, $D = 3$ (i.e. a uniform solid) have similarly simple values. More complex structures often have intermediate values that can be related to these simple geometries. The Koch Curve [36], commonly depicted as a line in 2D with fractally dense curves,

has a fractal dimension slightly more than that of a line in 2D ($D \approx 1.262$), since it fills space more completely. The freely jointed chain, a simple model for flexible polymers, is a random walk in 3D with a fractal dimension value intermediate between a volume and line ($D = 2$). Finite geometries (non-fractal) can be analyzed in the same way as fractal structures, though the range of consistent scaling is limited. Instead, the average mass-density at different size scales will fit a power-law trend when scaling is consistent. This can be applied to our coarse-grained simulation results. One formalism to quantify this is:

$$D = \frac{d\log L(r)}{d\log r}$$

for average mass L at radius r from any bead. This is closely related to the RDF $G(r)$, as the average mass in a space of radius r around a bead is:

$$L(r) = \frac{V}{N} \sum_{\rho=0}^{r} G(\rho)$$

When this technique is applied to the filament networks we report, in the very short range ($r < r_{min}$) the geometry of individual filaments is dominant ($D \approx 1$) and in very long range the space is filled volumetrically ($D = 3$). In the intermediate range, the scaling parameter will transition to an intermediate value that may be consistent over a decade. The locations of transition points representing the limits to the length-scale range of a structure can be identified by finding crossover points (i.e. points where D transitions from one value to another).

In Figure 6a, a power-law fit of the mass-scaling for the branching network in Figure 10 is shown with a scaling parameter of 1.3 in the intermediate region. The transition point where two power law fits meet represents the mesh size here. The system of isolated bundles in Figure 9 similarly has a transition point in its mass-scaling (Figure 6b) representing the size of a bundle. Diagrams representing the meaning of these values are shown adjacent in Figure 6c-d.

2.6 PERCOLATION ANALYSIS

An analysis of the connectedness of a simulated network is particularly useful for time-resolved studies of the evolution of the structure, and allows verification that the structure has evolved to a quasi-equilibrium state. A structure that appears well developed by its RDF may continue to evolve subtly by slowly forming a more connected structure while maintaining its general morphology.

In the evolution of a typical network structure, three distinct time-regimes are identifiable: rapid network formation, slow bundle thickening, and the quasi-equilibrated state. In the initial stage (rapid network formation) filaments quickly

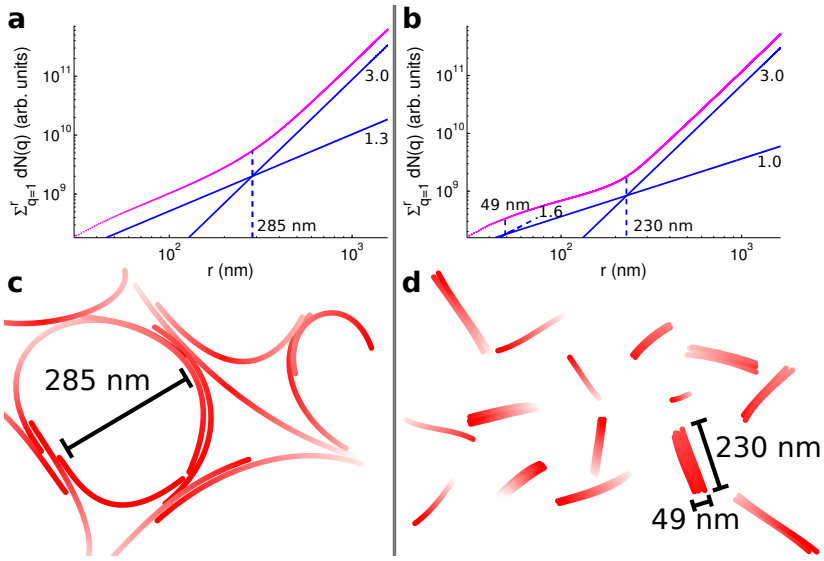

Figure 6: Mass-scaling of a branching network structure (a) and isolated bundles (b) with different transition points and scaling parameters. Diagrams representing the calculated values in each structure are shown (c-d).

form 'clusters' of interconnected (directly or indirectly) filaments. The average number of filaments in a cluster grows as separate clusters join, eventually forming a percolated structure with nearly all filaments connected to every other filament by cluster-cluster aggregation [8, 9]. Once the network structure is formed, loose ends of filaments continue to fluctuate, forming new connections as they are attracted towards other bundles. At the limit of this process, a quasi-equilibrium structure is formed which persists. This is seen experimentally with F-actin gels, which form a pseudo-stable gel rapidly [9].

To perform the percolation analysis, two parameters are calculated: the average cluster size and the average connections per filament (connectivity). In the first phase of this calculation, the inter-filament "cross-links" are identified by the proximity of close filaments. If any two beads on different filaments are within slightly more than the bond distance ($r_{min} + 1\,\text{nm}$), a bond is recorded in a symmetric logic table T. If filament number A is sufficiently proximate (cross-linked) to B, then $T_{A,B}$ is set to 1, otherwise it is 0. The logic table formed by repeating this check for every filament pair is an $N \times N$ symmetric adjacency matrix with all cells along the diagonal set to 1. Only the upper triangular part is used to prevent redundancy. By taking advantage of the MDAnalysis Python toolbox, this table can be formed efficiently.

As an example of this process, consider the example network graph in Figure 7 representing eight filaments with "cross-links" between them. The logic table representing this network graph is shown adjacent. Each diagonal cell uniquely rep-

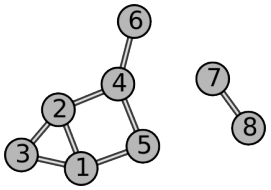

$$\begin{bmatrix} 1 & 1 & 1 & 0 & 1 & 0 & 0 & 0 \\ & 1 & 0 & 0 & 1 & 0 & 0 & 0 \\ & & 1 & 0 & 0 & 0 & 0 & 0 \\ & & & 1 & 1 & 0 & 0 & 0 \\ & & & & 1 & 1 & 0 & 0 \\ & & & & & 1 & 0 & 0 \\ & & & & & & 1 & 1 \\ & & & & & & & 1 \end{bmatrix}$$

Figure 7: An example network graph and corresponding adjacency matrix. The network has an average connectivity value of 0.609 and average cluster size of 0.625.

resents a node/filament, while off-diagonal cells represent connections between nodes/filaments.

In the second phase of calculation, a recursive algorithm parses this logic table incrementing a counter for each value. The recursive algorithm is simply stated for any cell $T_{i,j}$:

- If $i = j$, increment the cluster size counter
- If $i \neq j$, increment the connectivity counter
- Set $T_{i,j} = 0$
- For each cell $T_{i\prime,j\prime} = 1$ such that $i\prime = i$ or $j\prime = j$ (on the same row or column), recurse from that cell.

The recursion is initialized from each cell on the diagonal, each time with the original copy of T. After recursion collapses, the cluster size and connectivity counters are normalized by the maximum value of cluster size, N^2. This recursion thus follows the connections between nodes, going deeper into the network graph with each depth of recursion until a full cluster is parsed. Since each diagonal cell parsed represents a filament connected (either directly or indirectly) to the cluster which includes the initialized node, by counting these diagonal cells the size of the cluster can be determined. Similarly, counting off-diagonal cells gives a measure of how well connected the cluster is. A more dense adjacency matrix will then have a higher connectivity value, while a more sparse adjacency matrix will have a lower connectivity value. A minimally connected full network (ring topology) would have a normalized connectivity value of 1, thus values greater than 1 are easily possible.

An example of this recursive algorithm is represented in Figure 8 for the network shown in Figure 7. Recursion is initialized at cell $T_{5,5}$ (representing node 5) as an example. At the top depth of recursion (red), $T_{5,5}$ is set to 0, and the cluster size counter is incremented once. The four nonzero cells in the row/column begin the next depth of the recursion (shown as dark blue). Cells in the same rows/columns are again parsed (light blue) looking nonzero values for the next

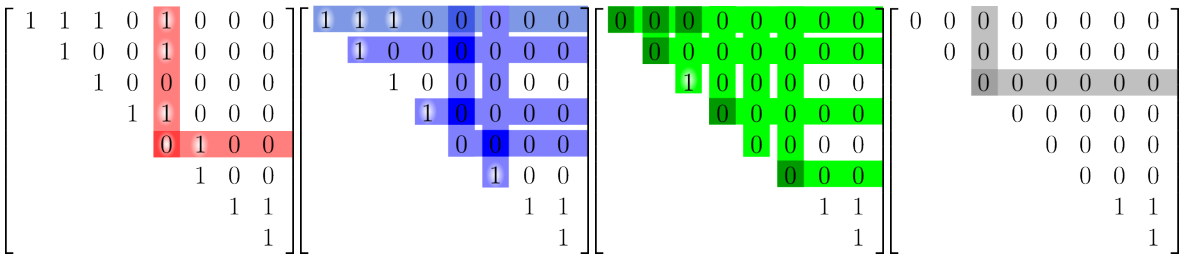

Figure 8: Example steps in computing connectivity and cluster size for the network in Figure 4 initialized from node 5. Recursion depth is represented as different colors (increasing from left to right). Dark colored cells represent points of recursion, while light colors represent cells parsed for the next depth of recursion. Parsed 1's continue the recursion procedure. Same-depth recursion is shown in parallel here for conciseness, while a series programming approach is necessary to prevent double-counting cells.

depth of recursion etc. At this depth, the cluster size counter is incremented twice, while the connectivity counter is incremented four times. In this case, recursion reaches a depth of 4. The remaining nonzero values represent nodes 7 and 8, which are unconnected to the larger cluster; they contribute nothing in this case.

The computational cost of this procedure scales poorly, with N^3. This can be improved by under-sampling the number of diagonal cells from which it is initialized.

3 RESULTS

3.1 STRUCTURAL PHASES

A number of distinct structural phases were identified in the parameter space investigated. These include primarily: isolated bundles, non-branching network, branching network, and knotted network (see Figures 9 and 10).

These phases each have distinguishing characteristics, as discussed in the following sections.

3.2 NOVEL STRUCTURES

Three novel structures were observed through exploration of the parameter space: the knotted network, the transverse network, and structural chirality. Structural chirality is not in itself a novel phenomenon, however our results present a novel understanding of its mechanisms.

3.2.1 *Knotted network structure*

The knotted network structure is particularly interesting as a novel structure, since it would likely be indistinguishable in microscopy from a branching network. The strongest distinction between these is the arrangement of filaments within bundles and nodes, of which the scale is too small for optical microscopy.

The knotted network structure shown in Figure 10 has the unique characteristic of having highly disordered binding within the dense network nodes. Similarly, tendrils frequently have a braided structure by which inner/outer filaments exchange places in a disordered way. This structure is observed in low L_P systems with long filaments and high r_{min}. The bundle cluster network structure discussed by Lieleg et al. [31] appears similar on the scale of the network, though that model does not include the woven structure observed. Since this phase was likely characterized based on optical microscopy, this may have been a suitable model based on that information; the knotted network model may be a more detailed model of this phase.

This structure additionally produces an average negative pressure in simulation, indicating that the knotting effect is pulling tendrils in as the nodes compact. Since the periodic box has constrained size, the filaments are then kinetically trapped in a conformation with stressed bond lengths.

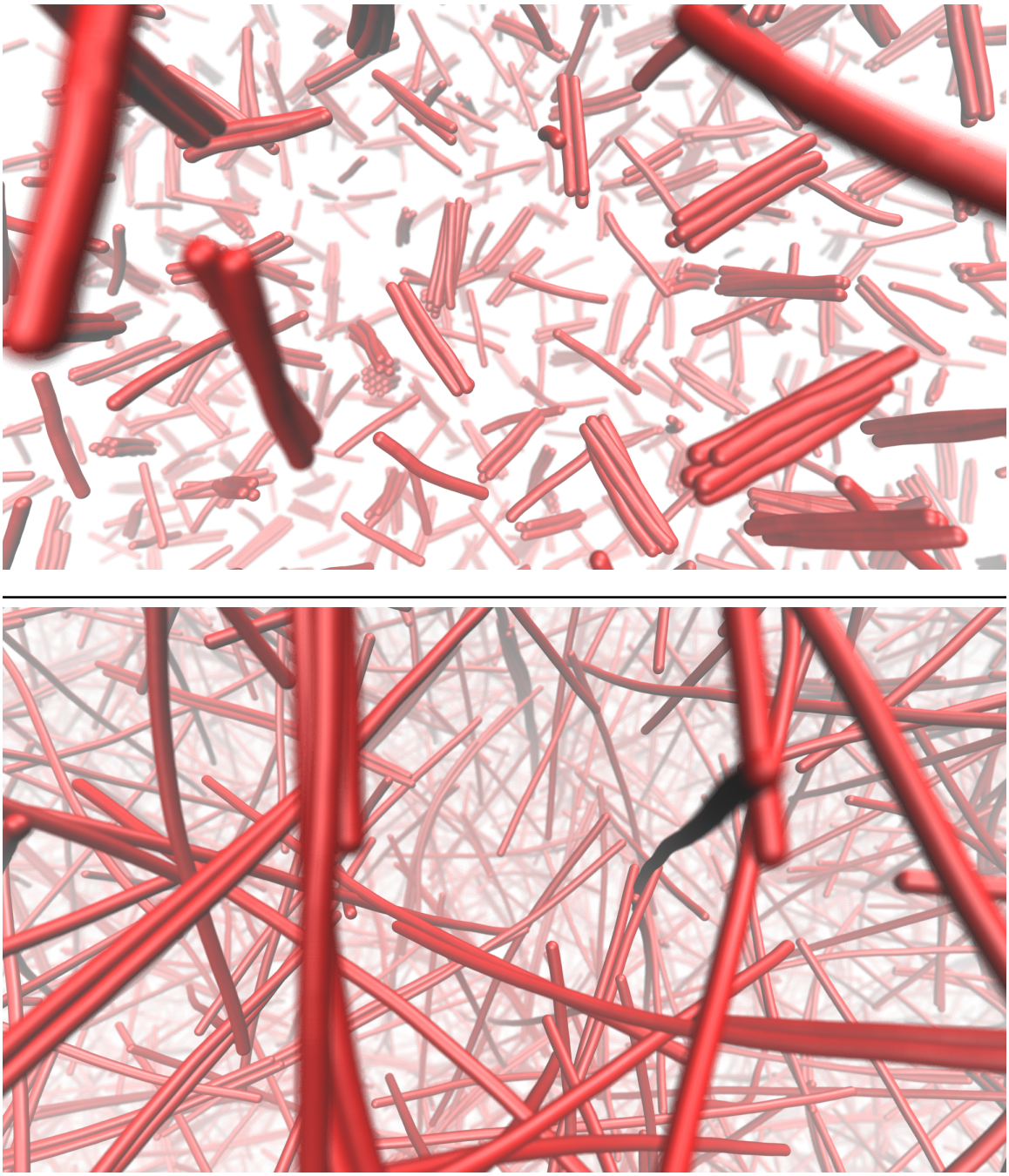

Figure 9: Two simulations snapshots: a system of isolated bundles (top, $L = 200$ nm, $L_P = 3.34$ µm, $r_{min} = 20$ nm) and a system of non-branching bundles (bottom, $L = 1$ µm, $L_P = 3.34$ µm, $r_{min} = 20$ nm).

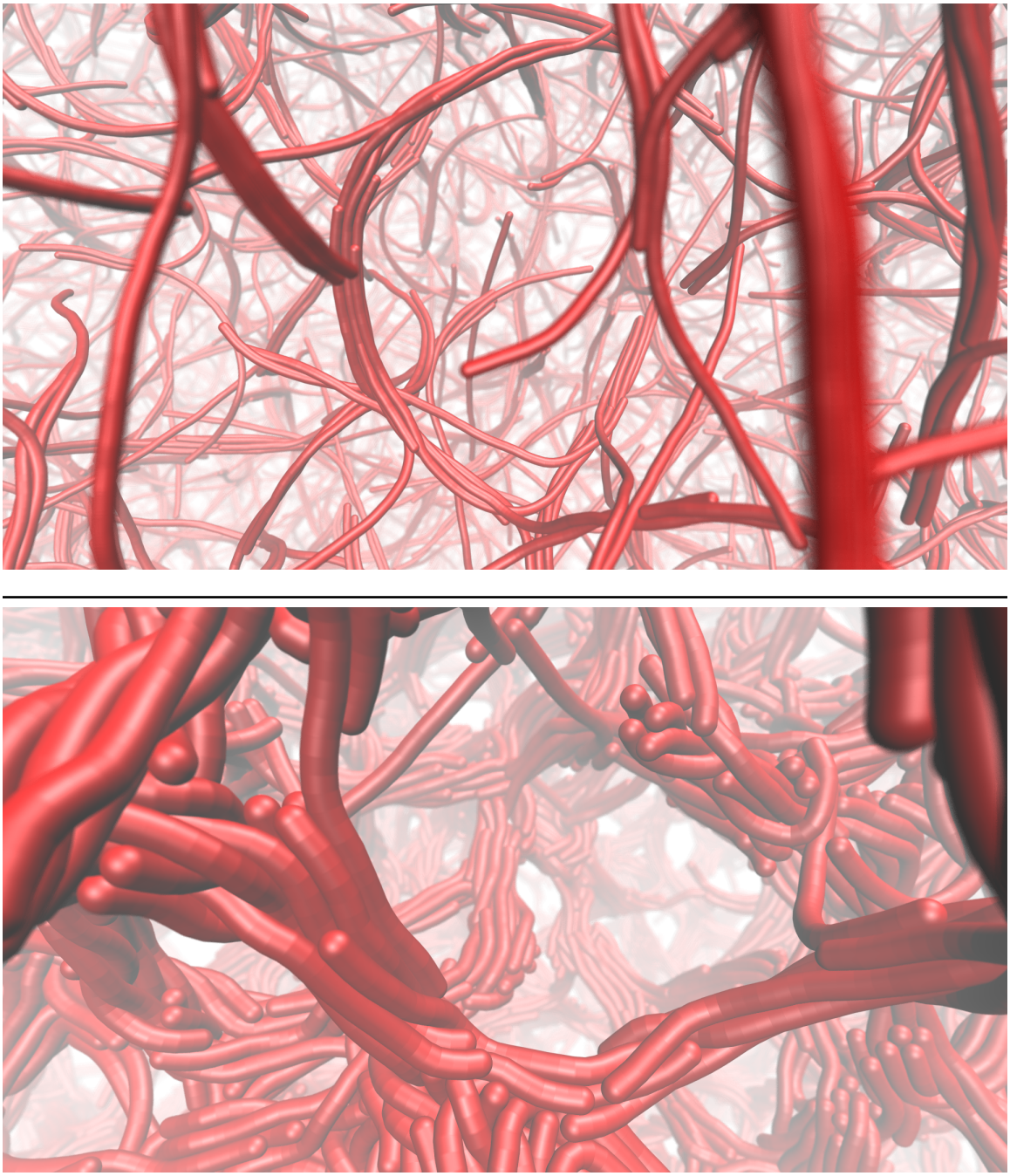

Figure 10: Two simulations snapshots: a system of branching bundles (top, $L = 1$ µm, $L_P = 3.34$ µm, $r_{min} = 20$ nm) and a knotted network (bottom, $L = 1$ µm, $L_P = 33.4$ µm, $r_{min} = 60$ nm). The apparent thickness of the knotted network in relation to the others is due to its r_{min} value.

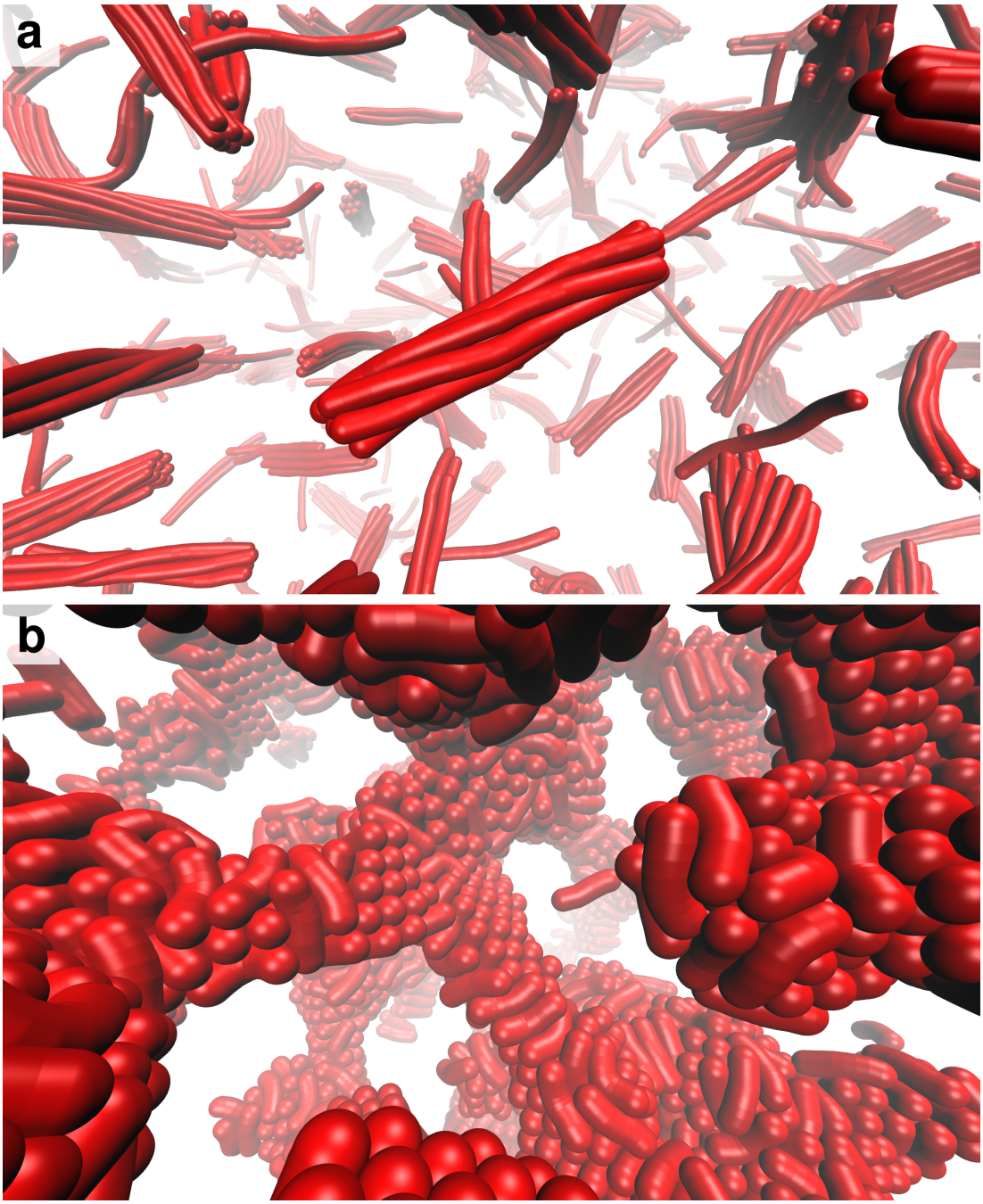

Figure 11: Bundle super-helicing was observed as in **a** for 400 nm filaments with $r_{min} = 30\,\text{nm}$. Transverse bundling was observed as in **b** with 200-400 nm filaments with $r_{min} = 100\,\text{nm}$.

3.2.2 *Structural chirality*

Chiral structure is innate to biopolymers, where super-helicing (helical structure from many chiral filaments) has been predicted [37, 38] and observed. Bundle helices (as shown in Figure 11a) were most strongly observed for 400 nm filaments with small L_P and $20 - 30\,\text{nm}$ r_{min}. This packing-induced chirality suggests that ex silico filament super-helicing is not necessarily a result of the geometric frustration caused by cross-linker/filament binding with helical polymer filaments. This effect may be induced with neither helical filament geometry nor discrete cross-linkers, but by simple energy minimization. Similar structural chirality has also previously been observed to emerge in simulations of discotic particles [39] and explored theoretically [37, 40].

3.2.3 *Transverse bundle network*

A novel transverse bundle network phase (as shown in Figure 11(b)) was observed when filament length L approached coaxial spacing r_{min} for short filaments. This phase exhibits tendrils between network nodes in which the filaments face orthogonal to the direction of the bundle.

3.3 HEXAGONAL PACKING STRUCTURE

It was observed that thick coaxial filament bundles also tend to form a hexagonal packing structure as indicated by correlation peaks in Figure 15. The 2D hexagonal filament packing structure is easy to identify by the ratios of the peak values: 20, 35, 40, and 53 nm (20, $20\sqrt{3}$, 40, $20\sqrt{7}$).

3.4 PHASE SPACE

To probe the impact of varying filament stiffness, binding distance, and length, an array of simulations was carried out. Figure 12 shows phase diagrams for four different attractive potentials with different r_{min} values. In each of these diagrams the strength of the potential ε was kept constant, but the position of the potential well is shifted in order to mimic cross-linkers of different lengths. We wanted to test the hypothesis that network structure is generally strongly dependent on filament spacing and flexibility as previously postulated for networks of actin bundles in the presence of α-actinin [23].

Of the tunable parameters of this system we have considered, two archetypes for effect were identified: complexity enhancing and network formation limiting. Length, concentration, and attraction strength are examples of the latter. At ex-

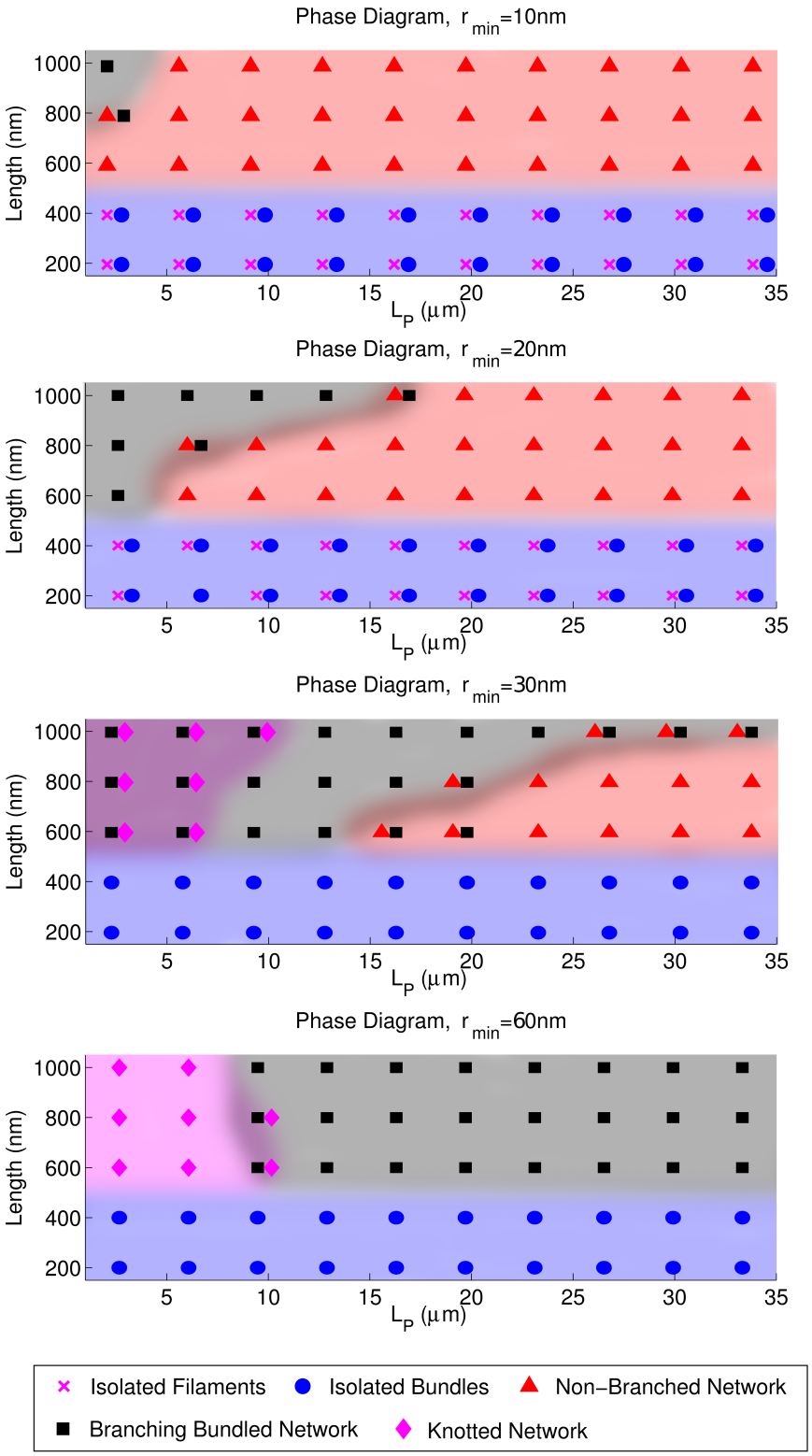

Figure 12: Phase diagrams for an array of simulations. Filament length L, persistence length L_P, and minimum coaxial distance r_{min} are varied for this set. Diagrams show phases for r_{min} of (a) 10 nm, (b) 20 nm, (c) 30 nm, and (d) 60 nm. Colors and symbols indicate the different phases, with a double symbol representing a mixed state.

treme values, the effects of network-limiting parameters can extend towards complexity enhancing. The complexity-enhancing parameters have no effect on network formation, however they dominantly control the complexity of the network structure generated.

3.5 HIERARCHY OF COMPLEXITY

The phase diagram (Figure 12) shows that semiflexible filament networks exhibit a hierarchy of complexity which can be traversed by strategically tuning select parameters. The hierarchy follows:

$$\text{Non-branching} \Leftrightarrow \text{Branching} \Leftrightarrow \text{Knotted}$$
$$\text{Low complexity} \ldots\ldots\ldots \text{High complexity}$$

One structure is more complex than another if it exhibits the same structural features of lower levels, with some additional structural characteristic. For example, the Knotted structure is a branching network with the added complexity of woven tendrils and nodes. Complexity-enhancing parameters influence these transitions.

3.6 FLEXIBILITY AND r_{min}

At the stiff end of the range (high K_B) non-branching networks occur, there is an intermediate range of flexibilities that favors the branching bundled network. At low K_B the network becomes highly entangled, forming unique knotted structures, where filaments twist together within the bundles and produce more complex, disordered structures (Figure 10). This series of phase diagrams also reveals how the phase sequence can be shifted by controlling r_{min}, providing a second degree of tunability to the system. As r_{min} is increased, filaments are forced to bind further apart. This increased filament spacing shifts the structural hierarchy towards the more complex structures, having an effect similar to an increase in flexibility.

3.7 LENGTH THRESHOLD

In all cases we can see that there is a threshold-like behavior for the formation of connected networks; both bundled and non-bundled networks only occur for filaments longer than 500 nm (also see Figure 13). This effect is independent of other parameters in the system. Above the length threshold, we can see a clear phase sequence as a function of L_P (or K_B). In the series of simulations shown in Figure 13, this transition point is identified as 500 nm. This transition is expected to be largely dependent on the global density of the system and attraction strength; L_P, ε, and r_{min} showed negligible effect on this value.

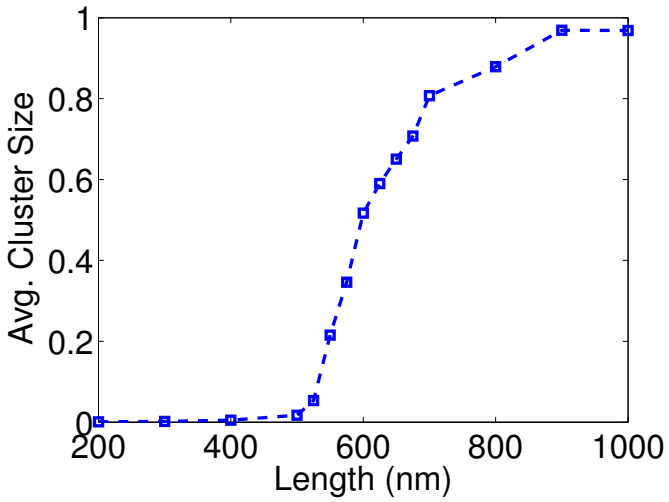

Figure 13: A comparison of average cluster size across different filament lengths for $L_P = 3.23\ \mu m$, $r_{min} = 20\,nm$. Network formation begins at 500 nm for this system.

3.8 DENSITY-SCALING FACTOR

Figure 14 shows a power law mass-density scaling analysis of three different phases: bundled network, isolated bundles, and non-bundled network. In Figure 14, graphs (a-c) show mass-density scaling for each structure (magenta/top) in comparison to slopes of fixed values (blue/below). For comparison, a system of rigid rods would yield a slope of 1 over a range where rod width $< r <$ rod length. A solid material of uniform density will give a slope of 3. The flexible Gaussian chain modeled in Figure 14(d) produces the expected fractal-like structure with a slope of 2 over two decades of r, validating the calculation method.

Results show that the structures in Figure 14 are uniform in density over longer length scales, tending towards a slope of 3 at 285, 230, and 229 nm respectively. Below this point we observe cross-overs to different scaling behaviors. Short filaments (Figure 14b) demonstrate typical scaling behavior for rigid rods, with a slope of 1 down to a length scale corresponding to the bundle thickness. In comparison, the branched and non-branched networks display similar structures with exponents of 1.3 and 1.4 respectively. Branching networks were observed to have a higher crossover when compared with the non-branched networks, indicating a larger mesh size.

3.9 RADIAL DISTRIBUTION FUNCTION ANALYSIS

The RDF emphasizes a few characteristics of structure: bundle thickness, bundle packing structure, and void-space size. In Figure 15 contrasts between the isolated

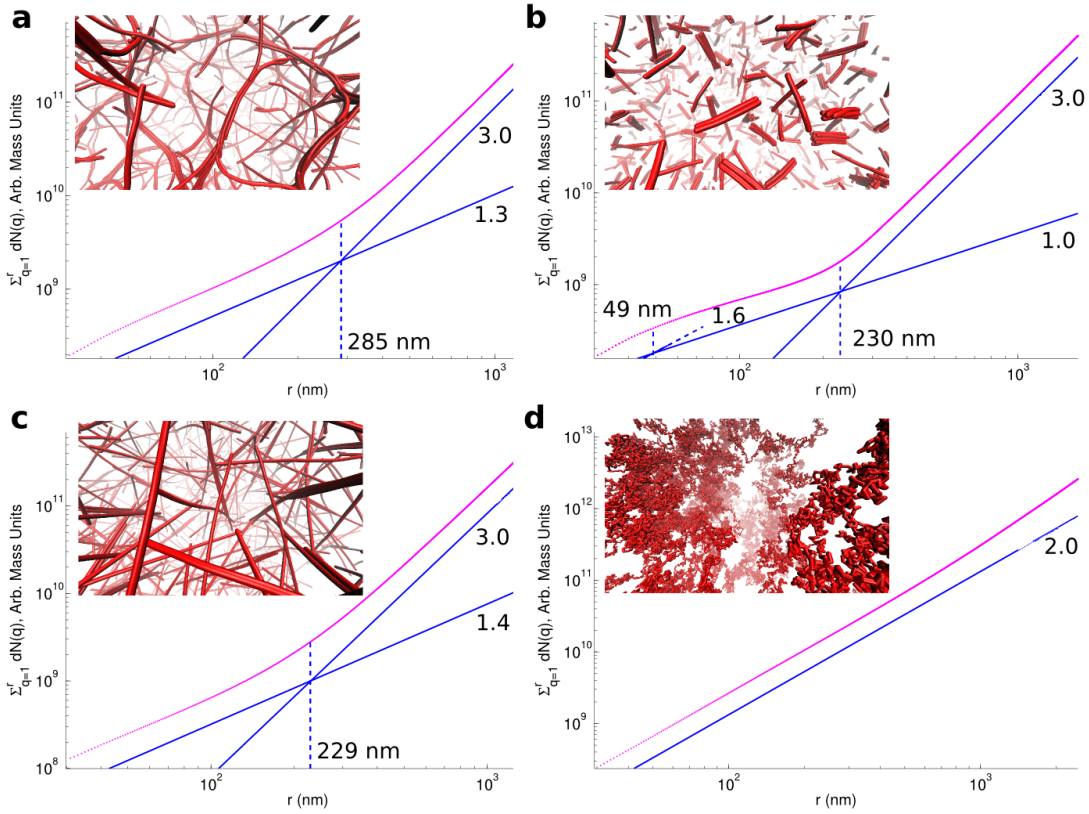

Figure 14: Mass-density scaling with power-law fits at various length scales. Plots (a-c) respectively represent structures shown in Figure 9 and 10. Plot (d) represents a freely jointed Gaussian chain model. Inset images show only a small section of the full structure for illustrative purposes. Filaments are represented in snapshots by the links between beads, showing the filaments' contours.

bundles, branching network, and non-branching network phases can be made by their RDFs. Short filaments form isolated bundles with many filaments per bundle, as represented by the high intensity of the low r peak. The packing structure of filaments is identified as planar-hexagonal by the peak ratios (see Section 3.3). The intermediate r region can have a RDF value less than 1, representing the typical void space at that radius by which the isolated bundles are separated (see Figure 15).

3.10 CONNECTIVITY ANALYSIS

It has been previously shown experimentally in the F-actin/α-actinin system that gels at high crosslinker concentrations will shrink after formation [8, 9]. This phenomena was attributed to the formation of additional connections after percolation. To investigate this hypothesis we carried out a connectivity analysis on

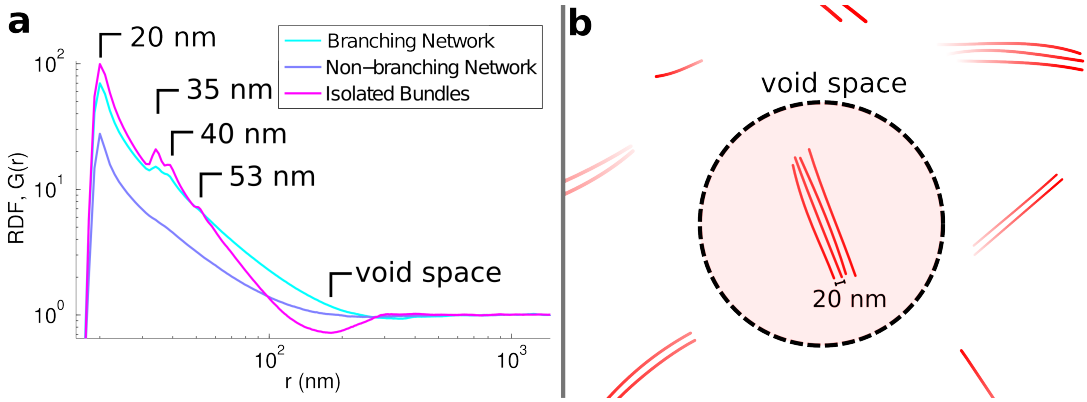

Figure 15: Selected RDFs (a) calculated for the three simulated network structures in Figures 9 and 10 with logarithmic axes. The adjacent diagram (b) demonstrates the void space where the magenta RDF drops below 1; this represents a lack of mass at this range characteristic of isolated bundles of filaments. Peak values are marked for the magenta and cyan RDFs.

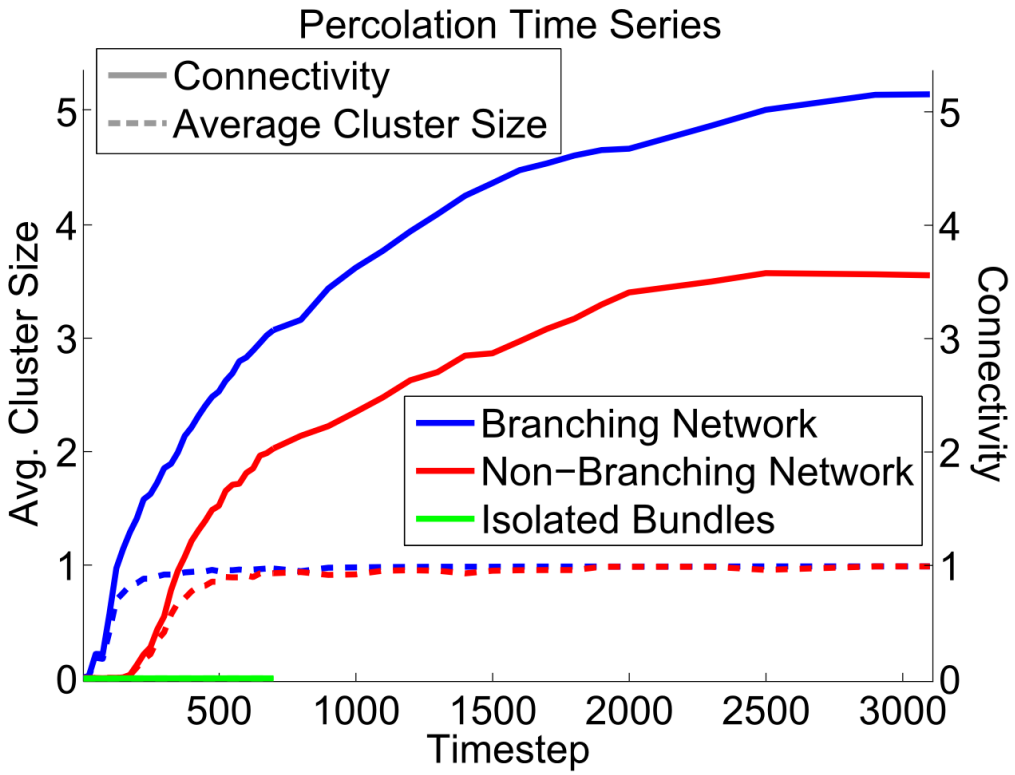

Figure 16: Simulations from Figures 9 and 10 characterized by percolation analysis (b) as a time-series. Solid lines represent connectivity; dashed lines represent cluster size. Data are shown for simulation parameters blue/triangle ($L_P = 3.34$ µm, $L = 1$ µm, $r_{min} = 20$ nm), red/circle ($L_P = 33.4$ µm, $L = 1$ µm, $r_{min} = 20$ nm), and green/square ($L_P = 3.34$ µm, $L = 200$ nm, $r_{min} = 20$ nm).

simulated networks in which cluster size and connectivity can be quantified over the simulation duration. Connectivity continues to increase after the system percolates, as filaments form more connected bundles, though network structure does not significantly change (see Figure 16). As can be seen in Figure 16, we find that connectivity continues to increase monotonically after the clusters reach a maximum size (where 1 represents a cluster spanning the simulation box). Isolated bundles have a low connectivity and cluster size because they do not form a network.

These results are consistent with experimental observations of contraction and gel "skin" formation [8, 9] in networks of F-actin bundles and suggest slow bundle thickening as free filaments connect with the network structure. We note that the effect is observed for both branched and non-branched networks in this system.

The dynamics of formation for the network of bundles show two distinct differences from the single filament network. The system percolates much more rapidly, and also makes more connections, plateauing at a higher connectivity (see Figure 16). This result can be easily explained by considering the structures shown in Figure 9 and 10. The single filament network does not form bundles and is constrained by its lack of filament flexibility once connections are formed. This limits the number of possible rearrangements at later times. The maximum connectivity reached is strongly dependent on filament flexibility.

This technique additionally highlights the minimum length required for network formation, as percolation only occurs above 500 nm (See Figure 13). The length threshold shows a dramatic transition to a percolated system, though length has a minor role past this threshold.

This result is significantly different from the results presented by Chelakkot et al., who observed nearly full independence of structure from filament length in Monte Carlo simulations of rigid rods with crosslinkers [41].

4

CONCLUSIONS

4.1 CONCLUSIONS

We observe for this semi-flexible filament system a hierarchy of complexity, Isolated Filaments (low complexity) $\Leftrightarrow$ Non-branching Network $\Leftrightarrow$ Branching Network $\Leftrightarrow$ Knotted Network (high complexity), dependent on L and L_P. The accessible phases are tuned by varying r_{min}, therefore network complexity increases with both flexibility and r_{min}. At high flexibilities, if the filament spacing approaches the persistence length, filaments are able to weave around each other to form a fascinating knotted network structure. Shorter filaments are limited by the range of space they can sample and do not form networks. These rules form a guide for structurally tuning the fundamental properties of engineered synthetic semiflexible filament polymers.

This investigation of semiflexible polymer structures is also documented across 2 publications [42, 43].

Part II

QUANTUM DOT/LIQUID CRYSTAL SELF-ASSEMBLY

Thermotropic liquid crystal provide an active basis for organization of nanoparticles. Using a bottom-up approach, nanoparticles well dispersed in the isotropic phase can be self-assembled by exclusion from the nematic phase as the material cools from the isotropic phase. A ligand exchange reaction can be used to create nanoparticles with mesogenic ligand coatings to allow better dispersion and assemble novel structures. Small angle X-ray scattering is used to inform the structure of a variety of materials which apply this design concept. These metamaterials have tunable properties with applications in quantum dot based electro-optic devices and more.

5 INTRODUCTION

5.1 INTRODUCTION

Liquid crystal/quantum dot composite materials are a promising area of research for devices with novel functionality and tunable optical properties. Materials formed from quantum dots exhibit properties unique from those of the individual particle; their strategic arrangement forms a meta-material. Liquid crystal provides a medium for assembly and/or reorganization of particles by its molecular switchability and orientational control. The composite mixture of liquid crystal and quantum dots is a promising material we have shown to generate unique structures.

5.2 MOTIVATION

A nanoparticle (NP) ensemble of may demonstrate collective behaviors different from the properties of its constituent particles [44]. Novel electronic, magnetic, and photonic properties[45, 46] result from the inter-particle spacing and interactions. The mechanisms for these novel material properties include plasmonic resonance for metallic NPs [47], superparamagnetism for magnetic nanoparticles (MNP)s [48], and Forster resonance energy transfer for semiconductor/quantum dot nanoparticles [49]. The key to producing functional materials exploiting these effects is the controlled assembly of NPs; forming close-packed superlattices of NPs is important. quantum dot (QD) metamaterials are a current focus, due to both their additional size-tunable optical properties and their current uses in applications: opto-electronic devices, [50] bio- chemical sensors, [51] photovoltaics, and as labels for biological microscopy [52]. Progress in QD superlattice formation may provide enhancements to these current applications. Combinations of MNPs and QDs are also an attractive combination, with great potential for application in both computing and biomedical science. As a magnetic/semiconductor hybrid material, this combination may be applied to computing to allow both data storage and processing within the same material [53]. In biomedical science this mixture may be applied to multimodal imaging using fluorescence and magnetic properties [54, 55].

The use of a host liquid crystal (LC) has potential for additional benefits as well. Since the LC director can be manipulated by electric or magnetic field, reorientation of structure or switchable devices may be developed around these materials.

5.3 BACKGROUND

The properties of the LC and QD components are key to the understanding of the formation and functionality of the composite mixtures studied. A brief discussion of the behavior and inherent properties of these components is presented here, as well the small angle X-ray scattering (SAXS) characterization technique I used.

5.3.1 *Liquid crystal (LC)*

A wide range of materials classify as liquid crystals, with a variety of molecular shapes, phases, and transitions. The defining property of this class of soft material is the presence of at least one short-range-ordered phase between the isotropic liquid and crystalline phases. This is a consequence of the molecular anisotropy of the particle, as thermal fluctuations and energy-minimizing structural order seek balance. Liquid crystal materials also typically exhibit birefringence due to the anisotropy of their molecular shape and orientational switchability by electric field due to the anisotropy of their charge distribution. The combination of these unique optical and electrical properties have made them a popular material for study and application, as well as an essential component of everyday consumer devices: the liquid crystal display (LCD).

A LC may exhibit a variety of phases. Two types of phases are of particular interest in this dissertation. In the isotropic phase a LC acts as a liquid with no orientational or positional order between adjacent particles. In the nematic phase LC particles have no positional order, but have directional order. The localized directional preference of a LC is termed the LC director. A thermotropic LC transitions between these phases at a specific temperature. A typical LC features a rigid part (mesogen) which induces structural order and one or more flexible parts which induce fluidity. The competing interplay of these effects allows LC molecules to have both behaviors.

Nanoscale particles can be dispersed in a LC host solvent by attaching ligands to their surface which limit aggregation. As the transition from isotropic to nematic occurs, solvated particles are excluded from the nematic phase while it grows. When the last of the nematic phase completes its transition, particles from the surrounding volume will have formed an aggregate. Our research utilizes this effect to create soft reversible, switchable metamaterials using quantum dots and magnetic nanoparticles.

The work to be presented here uses the rod-like thermotropic LC 4-Cyano-4'-pentylbiphenyl (4-Cyano-4'-pentylbiphenyl (5CB)) which transitions between isotropic and nematic at 36°C.

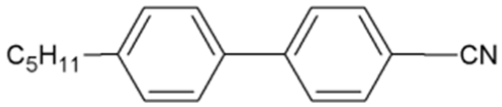

Figure 17: Chemical diagram of the liquid crystal 4-Cyano-4'-pentylbiphenyl (5CB) used as the host solvent for these materials. Its phase sequence is $K \xrightarrow{20.5} N \xrightarrow{36.0} I$.

5.3.2 *Quantum dots (QDs)*

Quantum dots are semiconductor particles which exhibit quantum mechanical properties due to the confinement of excitons within their ~10 nm size. The confinement of excitons within this small space creates quantized energy levels which can be modeled as a particle-in-a-box [56]. Applying this model, the energy levels can be shown to vary with $1/L^2$, creating a strong size dependence for the band gaps. This relationship allows QD materials to have optical properties tunable by the particle size. For example, CdSe QDs can be tuned to have peak emission anywhere in the visible spectrum.

The work to be presented here uses CdSe/ZnS (core/shell) quantum dots due to the tunable range of their emission wavelength, from 450 to 650 nm. These QDs are initially coated with octadecylamine surface ligands (NN Labs); a ligand exchange functionalizes the surface by replacing these with mesogenic LC ligands in some materials.

5.3.3 *Magnetic nanoparticles (Fe_3O_4 NPs)*

Nanoparticles (NPs) are a group of particles diverse in composition and morphology which exhibit electronic, magnetic, and optical properties unique to their small size due to quantum confinement. Patterned arrangements of these particles form meta-materials with modified properties and functionality. Magnetic NPs exhibit these effects while additionally manipulable by external magnetic field due their superparamagetism.

The work to be presented here uses Iron(II,III) oxide (Fe_3O_4) MNPs (NN Labs).

5.3.4 *X-ray scattering techniques*

In this dissertation, small angle X-ray scattering is used to investigate the structure of QD-LC composites. In order to understand the principles of SAXS, it is best to relate them to X-ray crystallography, as the physical processes are identical; they differ only in the description of the material studied. These principles are more easily conveyed in relation to a well-ordered crystalline material.

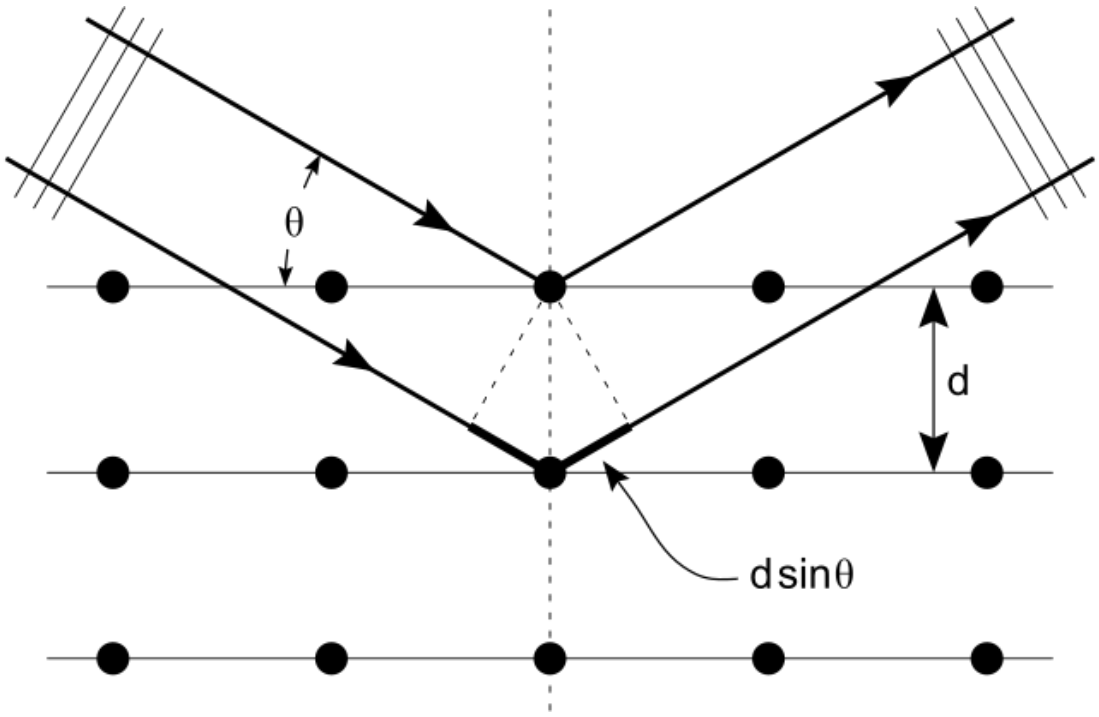

Figure 18: A square lattice diffracts X-rays incident from the left. When the Bragg condition ($n\lambda = 2d\sin\theta$) is satisfied, constructive interference creates a reflection at 2θ from the incident beam. "Bragg diffraction illustration" by Hydrargyrum is licensed under CC BY 3.0.

5.3.4.1 *X-ray crystallography*

A crystalline material has well ordered structure and repeated lattice spacings which diffract X-rays. Crystallography applies X-ray diffraction to measure these repeated spacings. An intense, coherent, collimated beam of X-rays elastically scatters by free electrons of the material (Thomson scattering). When the Bragg condition (see Figure 18) is satisfied, the scattered X-rays interfere constructively, forming a coherent reflection at 2θ from the incident beam. The reflection angle relates to the d-spacing of the repeating structure from which it scatters.

Bragg's law defines this relationship between the wavelength λ of the incident beam, lattice spacing d, and reflection angle 2θ:

$$n\lambda = 2d\sin\theta$$

For a crystalline material, long range order results in many orders of reflections, with reflection indices n. These reflections are typically observed/recorded on a flat ccd area detector, producing a diffraction image as in Figure 32. A crystalline powder, which would contain many crystalline grains with random orientation, results in a diffraction image of concentric rings.

5.3.4.2 *Small angle X-ray scattering (SAXS)*

The SAXS technique applies the same physical principles of crystallography with two caveats relating to the material subject of study. The eponymous difference in SAXS is that the scattering angle is typically small, ~0.1-10° (representing length scales on the order of ~5-100 nm). This angle range defines the limiting resolution, along with the available beam energy.

Considering the bounds of resolution with SAXS, materials of interest are often particles or macromolecules in solution. Therefore, in contrast to crystalline materials, the typical subject of study for SAXS also has weak long range order, resulting in less coherence at higher orders (n). Additionally, much like a crystalline powder, all possible orientations contribute to the diffraction image. Structurally complex materials (such as the LC-QD shells discussed later) may have preferred orientations, resulting in either polycrystalline 'rough' rings or simpler directional preference in the diffraction image.

The d-spacings represented through SAXS are often more like average interparticle spacings rather than spacings between lattice planes. As such, it is better described as a 'scattering' technique instead of 'diffraction', the latter implying long-range order. SAXS is typically weaker and more diffuse than Bragg diffraction. Characteristic peaks observed with SAXS are usually broad due to disorder in the materials. Many materials exhibit no peaks at all, however interesting information can be gained from fitting the scattering curve to obtain mass scaling data as a function of lengthscale, much like the power-law fit mass-density scaling technique applied in the first part of this dissertation.

5.3.4.3 *Synchrotron radiation lightsources*

An X-ray source suitable for SAXS must have specific properties difficult to sufficiently produce outside of large user facilites such as the Stanford Synchrotron Radiation Lightsource. The source beam must be monocromatic, coherent, and collimated. Additionally, a high brilliance X-ray beam is desired to reduce the scan time required and improve statistics. With non-synchrotron experimental setups, the brilliance of the source is often a limiting factor due the weak scattering of soft material.

A synchrotron lightsource satisfies all of these criteria. At a synchrotron facility, a large storage ring maintains a consistent beam of electrons. At insertion points along the ring, a series of alternating magnetic fields periodically deflect the beam; the change in momentum of the electron beam is related to a release of photons with energy matching the change in kinetic energy of the electrons. The physical mechanism for this release of photons as a result of accelerating relativistic charged particles is known as synchrotron radiation (similar to cyclcotron radiation and Bremsstrahlung). The released photons are focused and/or collimated and filtered to be monochromatic.

A vacuum is maintained for the beam path to minimize scattering with air. The X-ray beam path enters a hutch at one end, and leaves the vaccum at an outlet covered by a window material which scatters minimally at angles of interest (i.e. Kapton, Mylar). As close to the outlet as is reasonable, the sample material is exposed to the X-ray beam. The beam then enters a vacuum pipe inlet on the far side of the sample, and continues towards the area detector on the far end of the hutch. A beam-stop is used to block the direct path of the beam, which would saturate and/or damage the detector due to the high brilliance of the beam, most of which passes through the the sample directly.

5.3.4.4 *Interpreting diffraction images*

In addition to the data contained in a diffraction image, a few experimental values are key to relating a spatial position on the detector to a measured spacing. The beam energy/wavelength (λ) and the sample-to-detector distance ('camera length') L are required. For any position on the detector a distance r from the beam-center, the scattering angle θ is given by:

$$r = L\tan 2\theta$$

Combining this expression with Bragg's Law, the scattering vector q is obtained:

$$q = \frac{4\pi \sin\theta}{\lambda}$$

This is the value typically reported when representing characteristic spacings because it both provides an easy connection with the diffraction image (low q near the center) and combines details of the experimental setup into a unified quantity. The scattering vector is typically reported with reciprocal-space units of Å^{-1}, however the characteristic real-space d-spacing can also be simply calculated by:

$$d = \frac{2\pi}{q}$$

As a diffraction image is processed, converting detector positions to reciprocal q-space, radial integration is applied, averaging all values over a fixed r or q. This reduces the 2D image to an intensity plot over q. The original diffraction image is maintained for reference, since the intensity plot lacks orientational information relating to directional order.

6 METHODS

6.1 PARTICLE ASSEMBLIES

This series of projects have aimed to utilize the isotropic → nematic phase transition of a thermotropic liquid crystal host to soft template QDs and other particles in solution. Quantum dots, liquid crystal ligand quantum dots, and magnetic nanoparticles were used to form a variety of materials.

6.1.1 *Quantum dots assembled by host LC phase transition*

This material is a suspension of CdSe/ZnS (core/shell) QDs in 5CB. The QDs are coated with octadecylamine surface ligands to promote dispersion and homeotropic ordering at their surface. The thermotropic LC host is prepared at the isotropic phase initially to promote dispersion. As the suspension is cooled, crossing the transition from the isotropic to nematic phase, patches of nematic phase extend, excluding QDs into the remaining nematic region (see Figure 19c-j). As the LC host finishes its transition, the QDs are brought together, remaining in clusters at the LC defect points resulting from the gradual phase transition. This self-assembly is induced by the energy cost of deformation of the LC host surrounding each particle in an ordered phase; the LC surrounding each QD forms splay about the surface, creating a defect point as shown in Figure 19a-b. Excluding the QDs from the growing ordered phase is the result of delaying this energy cost and minimizing it to the remaining point defects around the resulting clusters.

6.1.2 *LC ligand quantum dots*

This material uses the same CdSe/ZnS (core/shell) QDs and 5CB host LC, however a ligand exchange reaction is performed to replace the ODA surface coating with a mesogenic LC ligand (see Figure 20). These dendrimer-like ligands have been shown to promote uniform dispersion in nematic phase LC [57]. The mesogenic ligand is allowed to align with the director of the ordered LC nematic phase, effectively shielding the surrounding LC from the splay condition for each QD. This dispersion is effectively maintained across the isotropic to nematic transition (see Figure 21).

At high concentrations, these LC-QD particles do form aggregate structures through the isotropic to nematic transition, however instead of simple clusters, the LC lig-

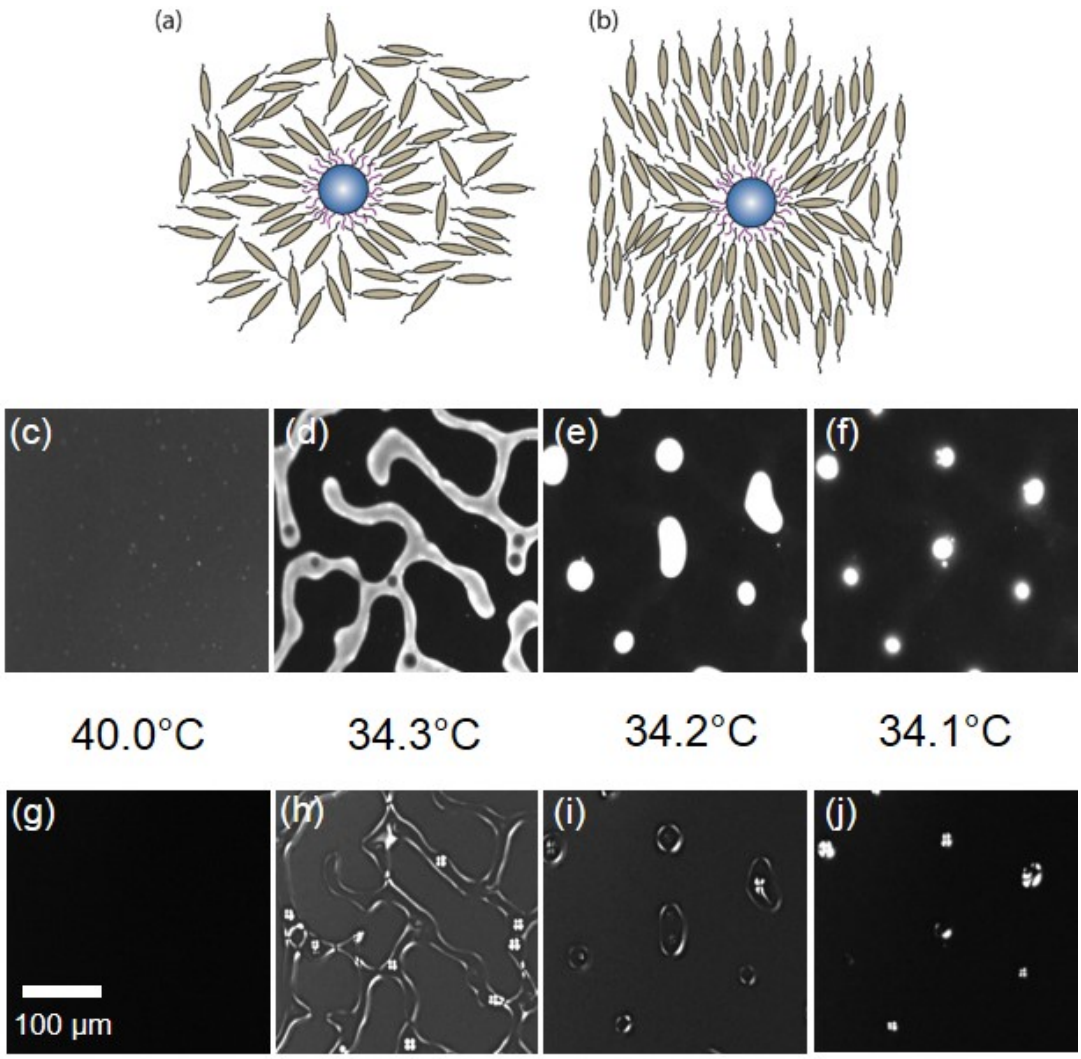

Figure 19: Diagrams represent a QD with ODA coating in an isotropic (a) and nematic (b) phase LC host. The transition from isotropic to nematic is represented by fluorescence microscopy (c-f) and polarized microscopy (g-j), cooling from 40.0°C to 34.1°C.

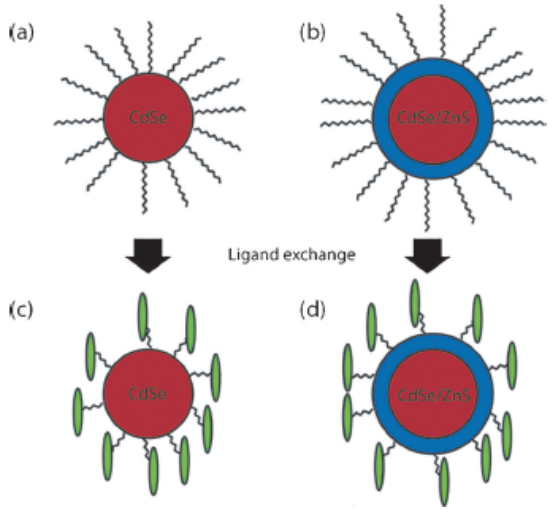

Figure 20: Diagram representing CdSe and CdSe/ZnS (core/shell) QDs (a-b) before and after (c-d) the ligand exchange. The non-mesogenic ODA ligand is replaced with the LC ligand.

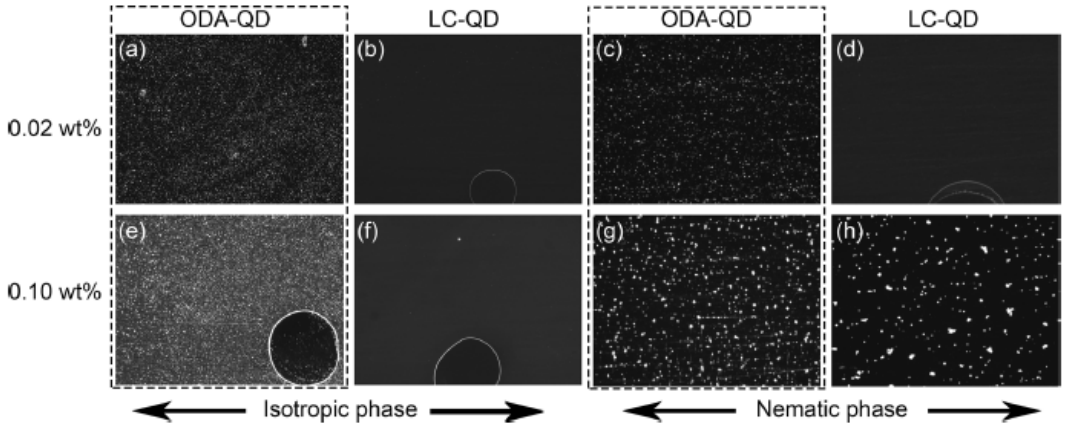

Figure 21: A comparison by fluorescence microscopy of ODA-QDs and LC-QDs at 0.02 wt% and 0.10 wt% in 5CB in the isotropic or nematic phase. The LC-QDs are more well dispersed, and dispersion is maintained across the isotropic to nematic transition. A higher wt%, the LC-QDs do aggregate through this transition, however instead of simple aggregate clusters, hollow shells are formed.

ands of adjacent particles form their own nematic-like ordered structure, inducing a more defined assembly. The structure formed by this assembly is a hollow spherical shell of one or more layers of LC-QD particles (see Figure 22), a completely novel formation. The spherical shape is a result of the self-assembly mechanism of the host LC bringing particles together into a shrinking sphere-like isotropic region. The structure of the particles and their interactions with adjacent ligands maintains the stability of this geometry up to 115°C.

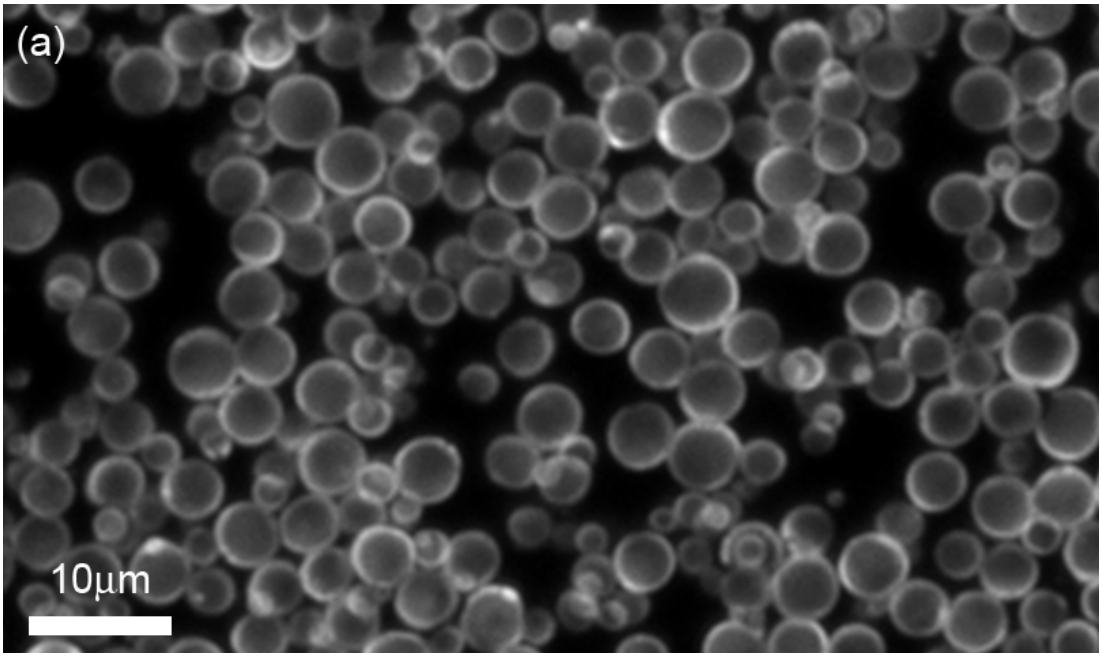

Figure 22: Fluorescence microscopy image of LC-QD shells with ligand L1 in nematic 5CB at room temperature.

6.1.3 *Magnetic NP and quantum dot composite*

This material is a mixture of CdSe/ZnS (core/shell) QDs with octadecylamine ligand coating and Fe_3O_4 magnetic nanoparticles with oleic acid ligand coating in 5CB. These MNPs are optically inactive, but superparamagnetic at room temperature. When added along with QDs to isotropic phase 5CB, a stable dispersion can be formed. After cooling through the isotropic to nematic transition, cluster aggregates of QDs and MNPs are formed by the same mechanism as the previous materials (see Figure 22).

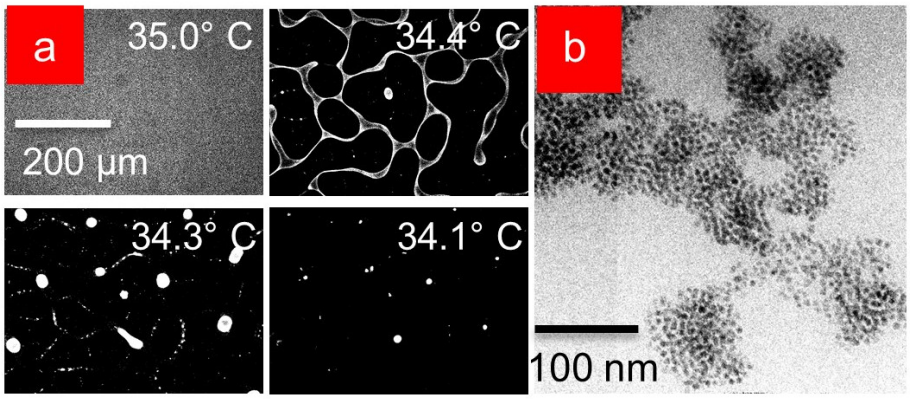

Figure 23: A mixture of 10 nm Fe_3O_4 MNPs and 6 nm CdSe/ZnS (core/shell) QDs in 5CB is cooled from the isotropic to nematic phase (a). A TEM image shows the packed structure of a self-assembled aggregate cluster formed by this method (b).

6.2 CHARACTERIZATION TECHNIQUE

A wide variety of characterization techniques have been applied to understanding these materials, including: magneto-optical Kerr effect confocal scanning, photoluminescence confocal scanning, confocal microscopy, fluorescence microscopy, transmission electron microscopy, and small angle x-ray scattering. The focus of my contributions to these projects was data collection and analysis by SAXS. This technique has great value for understanding QD-LC composites. It provides measurements of sub-optical resolution spacings. It also measures the structure of the bulk like a spatial Fourier transform. For these reasons, it serves as an excellent complement to the other techniques applied to studying QD-LC composites.

Data has been collected for these projects across four beamline runs, though I've participated in nine runs with the Hirst group.

6.2.1 *Small angle x-ray scattering*

The Stanford Synchrotron Radiation Lightsource beamline 4-2 was used to collect diffraction images for a variety of samples. A 9 keV, 1.7 m transmission SAXS setup was used. Samples were contained in sealed 1.5 or 1.0 mm glass or quartz capillary tubes. Beamline 4-2 features a Rayonix MX225-HE area detector. Diffraction images were radially integrated using Sastool.

A custom sample stage was developed for these experiments.

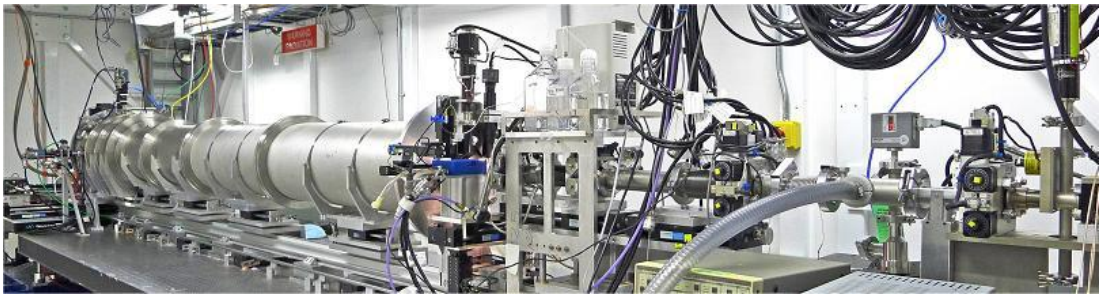

Figure 24: Beamline 4-2 hutch interior. The beam path follows the vacuum tube from the right through the sample chamber (not visible) to the area detector at the far left.

6.3 BEAMLINE APPARATUS

An aluminum block sample stage with a water channel for temperature control has been used to mount the sample capillaries for QD-LC composites. Additional features were required for the study of the LC-QD shells and MNP-QD mixtures. This section discusses tools and methods for beamline apparatus design. This should serve to provide a design basis for future apparatus development.

A beamline sample mount with specialized features was required for experiments performed at Stanford Synchrotron Radiation Lightsource (SSRL) beamline 4-2. This sample stage featured two goniometer axes and variable magnetic field control. Remote control of these features was desired so that the beamline hutch could remain closed between scans to save time. The design was limited to fit within the space between the two vacuum windows on either side, minimizing air scattering. Sample material was contained in glass/quartz capillaries with 0.01 mm wall thickness; these must be securely mounted without breaking. Limitations included a budget of ~$100 and timeline of 2 months.

Sample rotation controls were required in order to sample more of the crystalline texture present in some diffraction rings. The low-q diffraction rings observed with SAXS sample a very limited portion of reciprocal space, likely missing polycrystalline peaks when long-range directional order is present. The host nematic LC director of the materials investigated induces such directionally ordered texture in some polycrystalline diffraction rings.

An adjustable magnetic field was required to observe structural changes of FeO_3/QD mixtures as the applied field induces particle re-alignment. The beam path must be simultaneously unobstructed while the magnetic field is applied. A magnetic field strength on the order of 0.1 T was desired to assure significant influence of the FeO_3 particle alignment.

6.3.1 *Design solution*

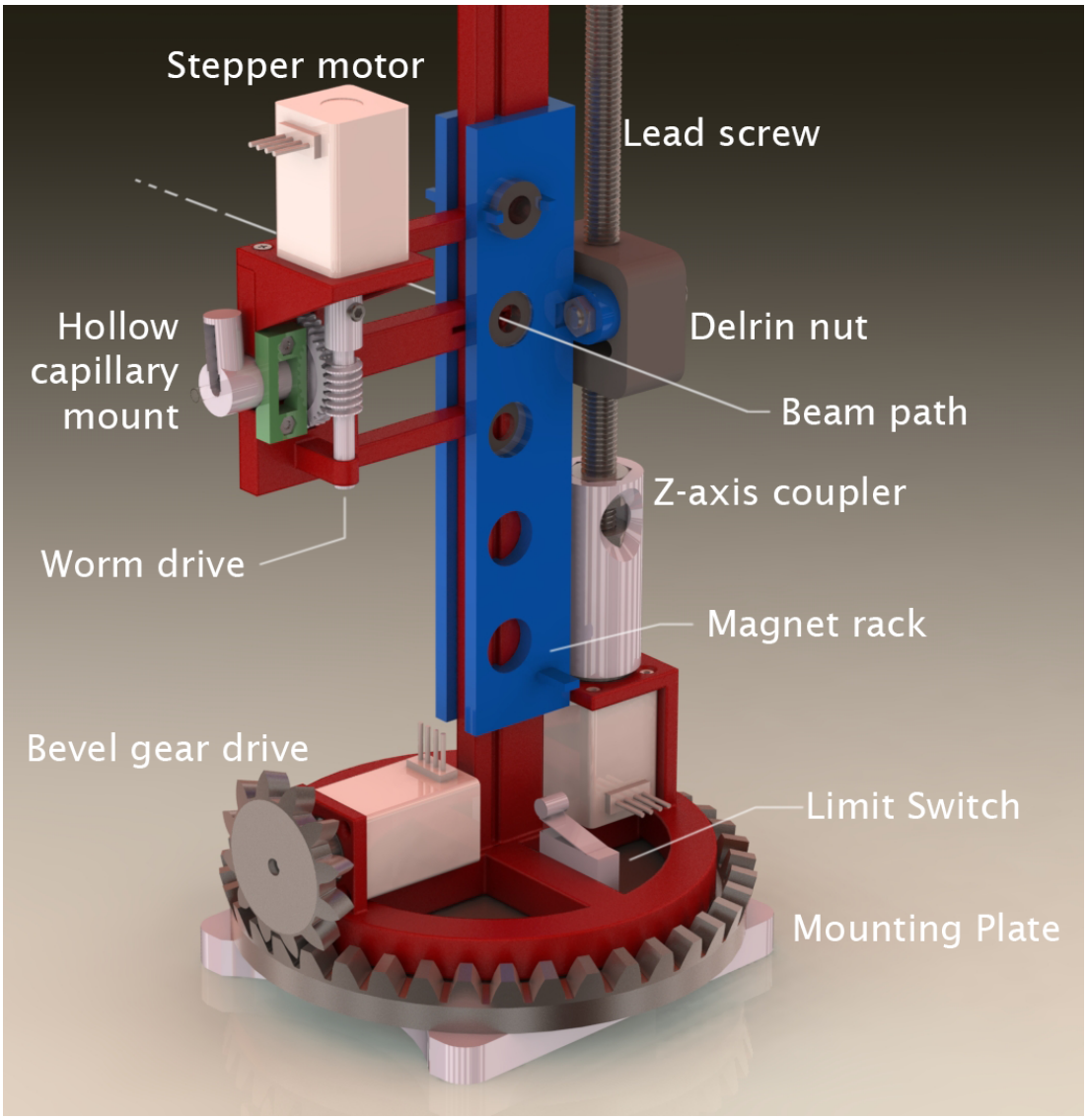

Figure 25: Diagram of components of the variable magnetic field sample stage.

The high design flexibility, low material cost, and rapid production time made additive manufacturing was well suited for this project. From the design concept, a complete 3D model was drafted in Solidworks which was split into smaller 3D-printable parts (see Figure 25). After printing, the parts were assembled using recessed nuts and screws (see Figure 28). Hot glue was used as a more permanent way of welding parts together, as polylactic acid (PLA) has a melting temperature similar to common high temperature hot-melt adhesives. An embedded Linux system approach was used, controlling a series of motors via intermediary driver chips using a Raspberry Pi.

The sample rotation was achieved by a Nema 8 stepper motor driving the rotation of a hollow sample mount via a worm drive for high precision. Capillary tubes can be inserted from the side into the hollow sample mount, and held in place by a small spring (see Figure 26). The tip of the capillary is exposed, centered on the beam path.

A series of ring magnets were secured in a vertically translating rack. Its translation was driven by a stepper motor coupled with an M8 lead screw. A delrin nut coupled the lead screw to the magnet rack to minimize backlash. These Neodymium magnets were arranged like a Helmholtz pair, with one on either side of the sample, coaxial with the beam path. This should provide a near-uniform field in the space between their centers. The magnet pairs have measured field strengths of 2340, 1436, and 494 G. A limit switch placed at the base of the stage provides a point for calibration and prevents crashing.

The stepper motors were connected to low-voltage stepper motor driver carrier breakout boards (Polulu DRV8834). A Raspberry Pi cobbler and protoboard connects the GPIO output pins of the Raspberry Pi to the stepper motor controllers (see Figure 27). Three pins from each driver are controlled as outputs of the Raspberry Pi: STEP (steps once on each pulse), DIR (direction of step), and $\overline{\text{SLP}}$ (holds the postion and allows stepping when held high). From the Raspberry Pi, these pins are software accessible binary digital outputs which can be pulsed/toggled to direct the stepper motors.

A simple shell interface was prepared in Python using the *cmd* module which allowed command based rotation and translation of the magnet rack. The Raspberry Pi was connected via ethernet cable to a laptop outside of the hutch. Using a Linux terminal, the Raspberry Pi could then be accessed remotely via secure shell (SSH) and the python shell interface invoked.

6.3.2 *Suggested improvements*

The 3D-printed PLA parts have a slight flexibility when printed thin. The tall and thin track which supports the sample mount is susceptible to flexing. If the alignment of the lead screw and stepper motor shaft is poor, it causes the sample mount to wobble as the magnet rack translates. The sample-detector distance and dependent calibrations are potentially sensitive to this. This wobble was minimized by creating a custom z-axis coupler which was carefully aligned and then in-filled with hot glue to create a pliable but well-aligned coupling. To better correct this, it is suggested a more rigid metal frame component be used to constrain the top end of the lead screw with a thrust bearing.

A second rotational axis was part of the original plan for this design. The purpose of the two-axis goniometer would be to more completely sample polycrystalline rings for texture analysis. This feature was planned for future studies. How-

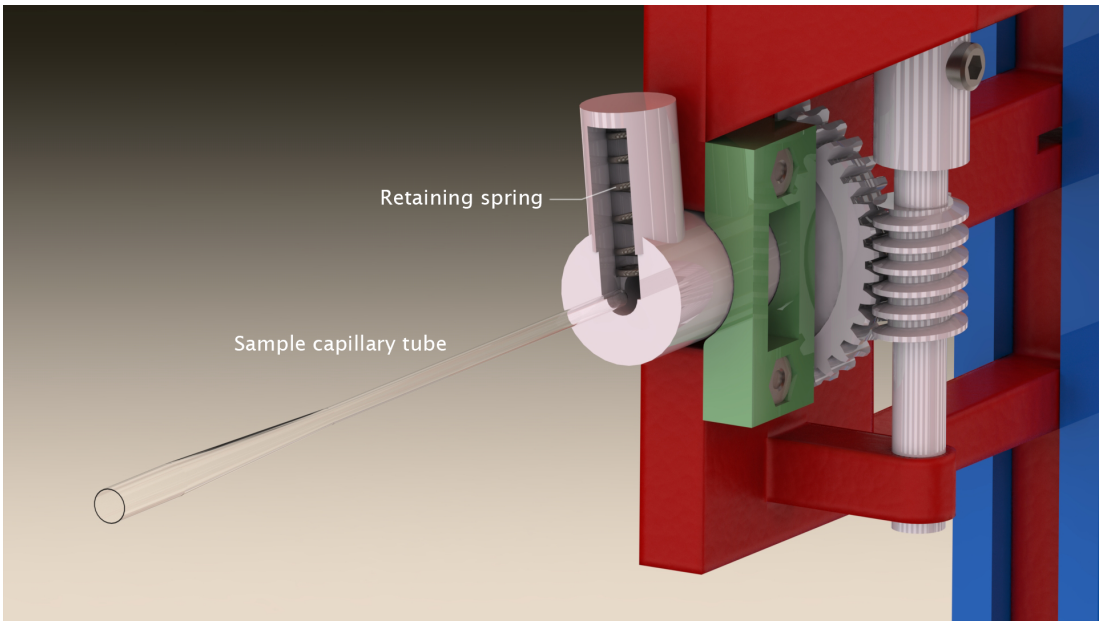

Figure 26: Diagram of the capillary mount. The worm drive shown rotates the capillary about its major axis.

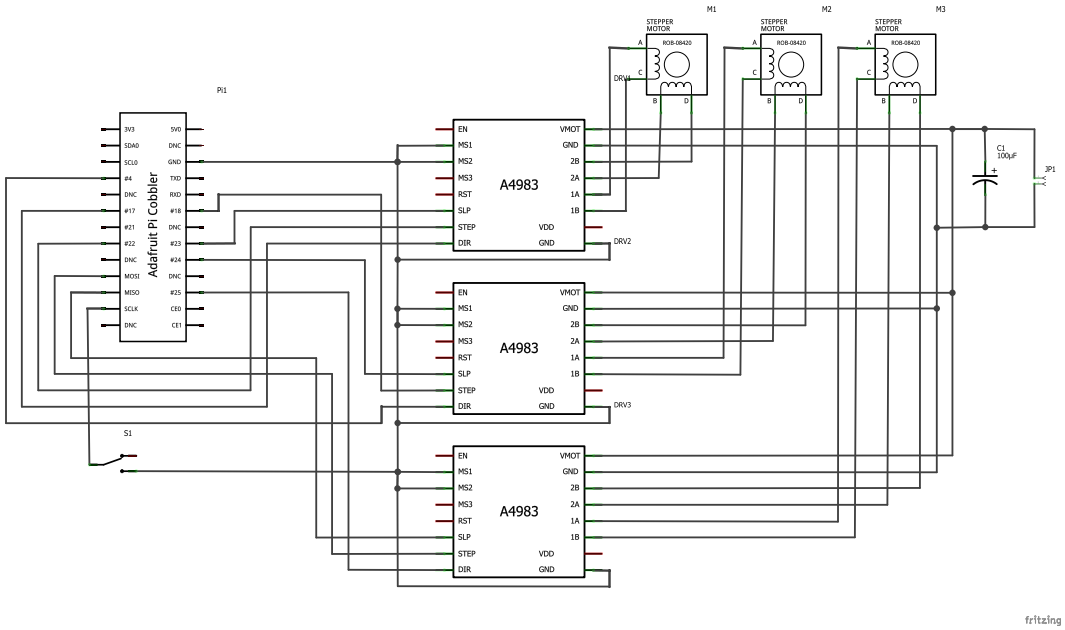

Figure 27: Circuit diagram for the variable magnetic field sample stage.

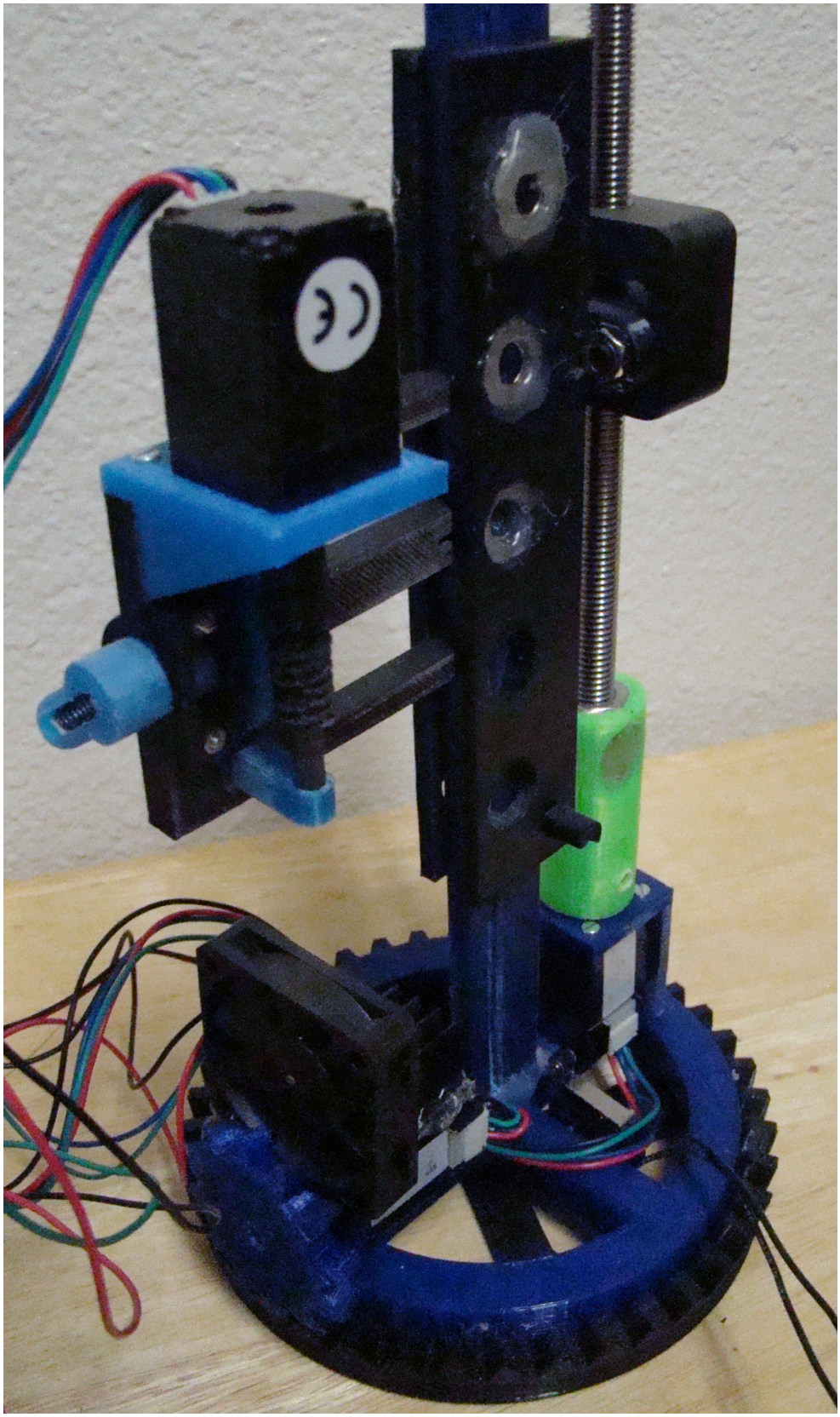

Figure 28: Rapid prototyped sample stage made from PLA plastic. Bolts would hold the black base to the optics mounting plate base.

ever, due to the small coverage of reciprocal space by low-q SAXS diffraction rings, many steps of rotations would be required to sufficiently sample the distribution of orientations. Additionally, since the design used a stepper motor to rotate the stage on the second (vertical) axis, and the cabling had a slight tension against this rotation, the position had to held in some way. To correct this, the design was adapted to have that stepper motor hold the position after rotating, though this was found to be impractical, since holding the position for long heats the stepper motor past the melting temperature of PLA. A better alternative is replacing this stepper motor with a servo motor, which have high holding strength due to their internal gearing ratio, as well as the inherent error sensing negative feedback which would resist any cable stress.

The capillary tubes used to hold sample material have some variablity in their diameter. This made mounting them an issue, since the mounting channel was too small for some capillaries and too large for others. A more gentle mount is suggest for future builds, utilizing either leaf springs or a foam ring on all sides of the open end of the capillary. Mounting capillaries horizontally also makes it difficult to keep the tip at a constant height when a too-thin capillary is inserted; the delicate closed end breaks easily. A vertical mount would solve these issues.

The protoboard was a cheap and effective way to connect the electronics together. For future projects, the circuit schematics made with Fritzing can be automatically drafted as a printed circuit board layout. From that layout a printed circuit board can be ordered, which would simply be a cleaner and more compact version.

This design also allows only one sample to be mounted at a time. In future designs, a well-plate array system like the one available at 4-2 would be valuable for automating high throughput data collection. The system available at 4-2 cannot use LC material due to its viscosity and cannot use toluene solutions due to the material used for its O-ring seals. However, it can serve as a model for a more versatile system suitable for our group's materials. A dual pneumatic/hydraulic system could draw material up like an air-displacement micropipette and then flush the capillary with toluene.

7

RESULTS

The SAXS results for these projects are presented here. A variety of other characterization techniques were used to analyze these materials; the results of these techniques combined informs the structure of these materials.

7.0.3 *Quantum dots assembled by host LC phase transition*

A SAXS analysis of the ODA-QDs in host 5CB LC samples was conducted at SSRL beamline 4-2. A characteristic spacing of 7.7 nm ($q = 0.128\,\text{Å}^{-1}$) was identified, matching the expected QD-QD spacing for a close-packed aggregate cluster (see Figure 29) [1]. The pure 5CB host LC has a broad directionally ordered peak as background relating to the average spacing between the LC molecules. This background is present at high q in the other materials investigated as well.

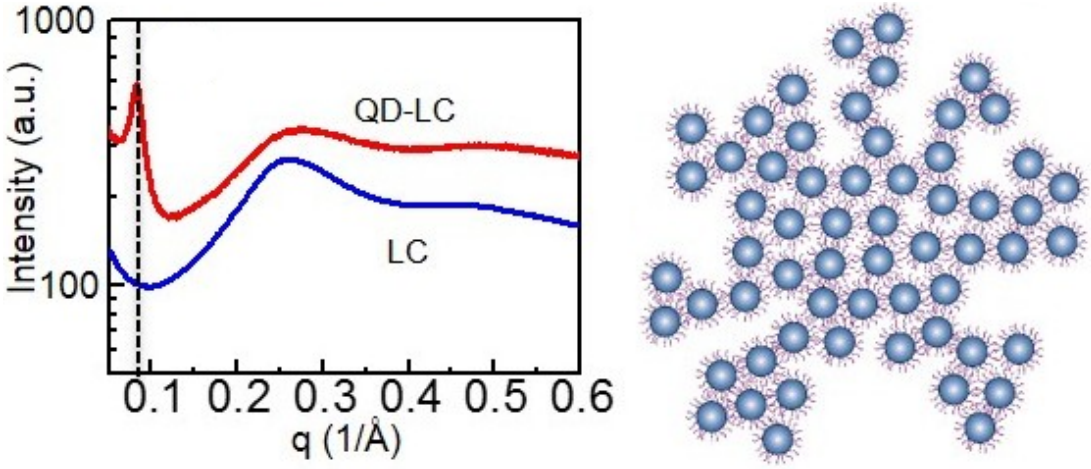

Figure 29: SAXS data (offset for comparison) showing the QD-QD characteristic spacing peak ($q = 0.082\,\text{Å}^{-1}$) and the LC background [1]. The diagram (right) represents the packed aggregate cluster structure expected.

7.0.4 *LC ligand quantum dots*

The LC-QD material was characterized using SAXS. At low-moderate concentrations, the ODA-QD quantum dots have an average spacing of 0.13 nm^{-1} (see Fig-

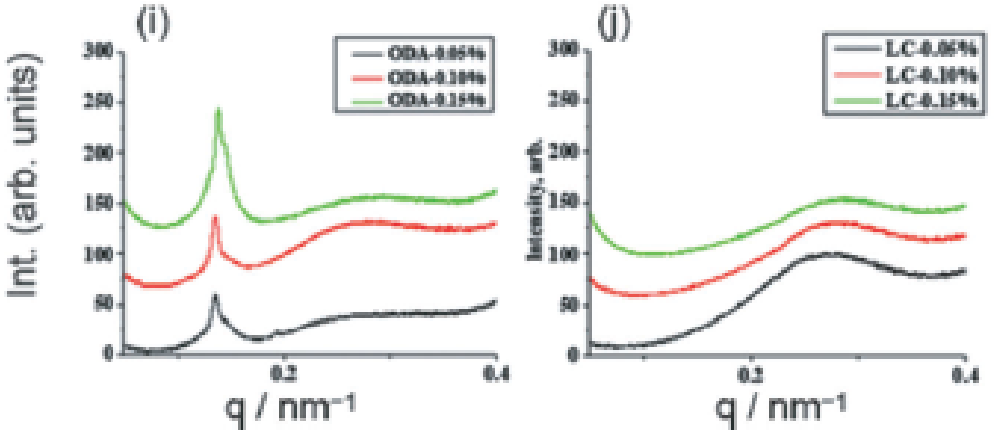

Figure 30: Comparison of SAXS data for ODA-QD and LC-QD at various concentrations [1, 2]. The QD-QD average correlation distance peak is absent for the LC-QD samples, indicating absence of aggregates, good dispersion.

ure 30). At the same concentrations, LC-QDs have no average correlation distance visible. This result indicates a great improvement to dispersion for the LC-QDs.

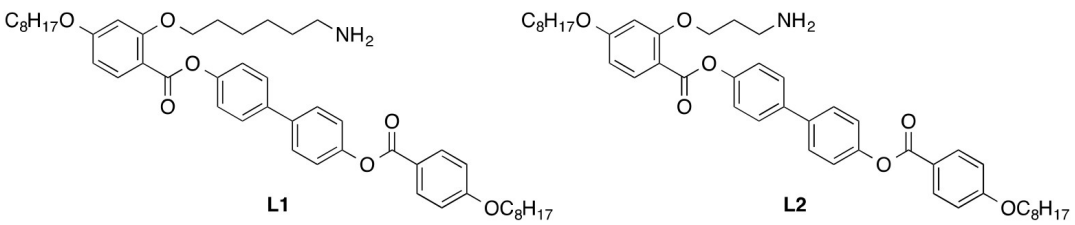

Figure 31: Molecular structure of the mesogenic LC ligands L1 and L2.

The hollow shell structure formed at higher concentrations of LC-QD particles was also investigated with SAXS. An example diffraction image is shown in Figure 32. Peak A ($q = 0.0616\,\text{Å}^{-1}$) represents a real-space distance of 10.20 nm, matching the expected average spacing between quantum dots packed in the shell wall [3]. This separation is slightly larger than the diameter of the QDs due to the addition of the LC ligand. The broadness of Peak A represents an average spacing without long-range order, matching observations made with TEM . The peak at position B is a sharp polycrystalline diffraction ring ($q = 0.128\,\text{Å}^{-1}$) representing a well-defined spacing of 4.9 nm. This length scale matches the length of the LC ligand rigid core, indicating localized crystallization of the ligand within the shell wall. Further support for this includes observations of the stability of the shell walls. The localized crystallization of the LC ligands would be the dominant structural component when their local concentration becomes dense enough to

form a well-ordered nematic phase of its own with neighboring particles, creating a self-sustaining spherical structure as aided by the LC phase transition.

When a mesogenic ligand with a shorter attaching arm L2 (see Figure 31) is used in place of L1, the QD-QD average spacing is shortened accordingly from 10.20 nm to 9.94 nm (see Figure 32). This change matches with the difference between L1 and L2, the truncation of three carbon atoms from the amine containing chain. This shows that the average spacing of QDs in the shell may be controlled by design of the material.

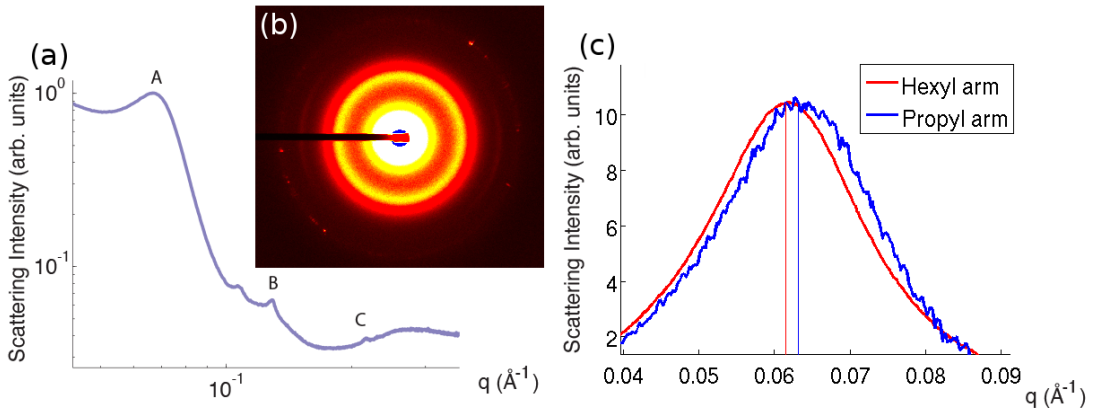

Figure 32: SAXS data (a) for LC-QD shells using L1 with its corresponding diffraction image (b) showing directional peak order and a comparison of the QD-QD spacing peak A (c) between ligand L1 (Hexyl arm) and L2 (Propyl arm) [3].

7.0.5 *Magnetic NP and quantum dot composite*

A series of SAXS experiments were completed to identify the structure of the composite cluster aggregates of MNPs and QDs self-assembled by host LC [4]. A range of particle ratios were investigated (see Figure 33), ranging from 3:1 to 1:10 (QD:MNP). At high/low ratios, only the structural characteristic spacing of the dominant particle is observed. The average characteristic spacings of these particles were 8.6 nm and 11.4 nm for the QDs and MNPs respectively, matching the expectation of a close-packed structure. An average spacing slightly greater than the particle diameter is a result of the ODA and oleic acid coatings. These average spacings are consistant across particle ratios. With intermediate ratios (1:1 to 1:2, QD:MNP), both characteristic peaks are present. These results indicate that the structure of the composite for intermediate particle ratios is aggregate clusters of segregated domains of QDs and MNPs. These results match with measurements made using magneto-optic Kerr effect (MOKE) and photoluminescence (PL) scanning.

Observations from PL scans showed a two- to three- fold increase in the peak emission intensity, however application of magnetic field showed no change in the characteristic spacings of these materials in SAXS. This indicates that the effect of applied magnetic field is compaction of the previously porous aggregate.

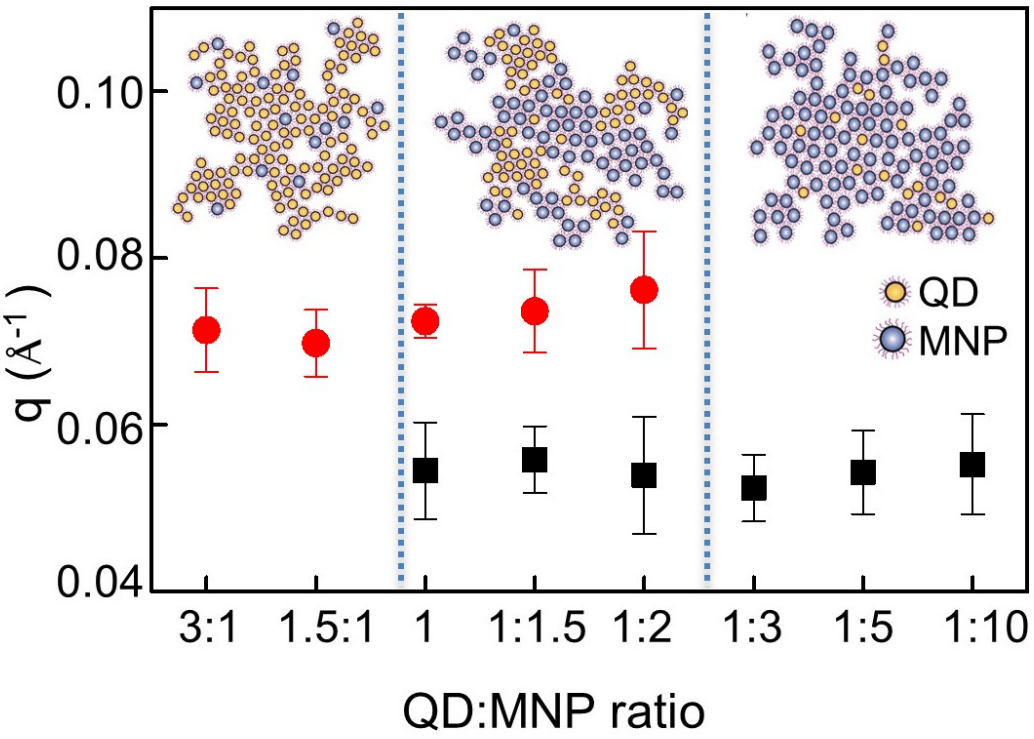

Figure 33: A mixture of 10 nm Fe_3O_4 and 6 nm CdSe/ZnS (core/shell) QDs in 5CB is cooled from the isotropic to nematic phase [4]. SAXS measurements identify the inter-particle characteristic spacings present, which are plotted here across different QD:MNP particle ratios. At intermediate ratios, characteristic spacings from the QD-QD spacing and MNP-MNP spacing are present. Diagrams represent the segregated domains of QDs and MNPs.

8

CONCLUSIONS

In these experiments, we have demonstrated the viability of using a thermotropic LC host actively to create ordered assemblies of nanoparticles. The isotropic $\rightarrow$ nematic phase transition of a LC is useful for this purpose. A material of ODA-QDs can be induced to form cluster aggregates. LC-QDs can be induced to form spherical shells. MNPs and QDs can be induced to form cluster aggregates with segregated domains. Additionally, our experiments with LC-QDs have demonstrated improvements to the dispersion of QDs in LC. Measurements by SAXS have been critical to determining structure of these materials, and supporting hypotheses made from observations by other techniques. The novel formation of LC-QD shells is of special interest for future work; a series of experiments have been planned as a continuation of this project.

The investigation of these QD-LC composites is also documented across 4 publications [1, 2, 4, 58].

BIBLIOGRAPHY

[1] Andrea L. Rodarte, Ronald J. Pandolfi, Sayantani Ghosh, and Linda S. Hirst. Quantum dot/liquid crystal composite materials: self-assembly driven by liquid crystal phase transition templating. *Journal of Materials Chemistry C*, 1 (35):5527, August 2013. ISSN 2050-7526. doi: 10.1039/c3tc31043d. URL http://pubs.rsc.org/en/content/articlehtml/2013/tc/c3tc31043d. (Cited on pages xviii, 52, 53, and 56.)

[2] Andrea L Rodarte, Zachary S Nuno, Blessing H Cao, Ronald J Pandolfi, Makiko T Quint, Sayantani Ghosh, Jason E Hein, and Linda S Hirst. Tuning quantum-dot organization in liquid crystals for robust photonic applications. *Chemphyschem : a European journal of chemical physics and physical chemistry*, 15 (7):1413–21, May 2014. ISSN 1439-7641. doi: 10.1002/cphc.201301007. URL http://www.ncbi.nlm.nih.gov/pubmed/24615927. (Cited on pages xviii, 53, and 56.)

[3] Andrea L. Rodarte, Blessing H Cao, H. Panesar, Ronald J. Pandolfi, Makiko T Quint, Lauren Edwards, Sayantani Ghosh, Jason E Hein, and Linda S. Hirst. Self-Assembled nanoparticle micro-shells tempated by liquid crystal sorting. *Soft Matter*. (Cited on pages xviii, 53, and 54.)

[4] Jose Jussi Amaral, Jacky Wan, Andrea L Rodarte, Christopher Ferri, Makiko T Quint, Ronald J Pandolfi, Michael Scheibner, Linda S Hirst, and Sayantani Ghosh. Magnetic field induced quantum dot brightening in liquid crystal synergized magnetic and semiconducting nanoparticle composite assemblies. *Soft matter*, October 2014. ISSN 1744-6848. doi: 10.1039/c4sm02015d. URL http://pubs.rsc.org/en/content/articlehtml/2015/sm/c4sm02015d. (Cited on pages xviii, 54, 55, and 56.)

[5] Harvey Lodish, Arnold Berk, S Lawrence Zipursky, Paul Matsudaira, David Baltimore, and James Darnell. *Molecular Cell Biology*. Freeman, New York, 4th ed. edition, 1999. (Cited on page 3.)

[6] Paul H J Kouwer, Matthieu Koepf, Vincent a a Le Sage, Maarten Jaspers, Arend M van Buul, Zaskia H Eksteen-Akeroyd, Tim Woltinge, Erik Schwartz, Heather J Kitto, Richard Hoogenboom, Stephen J Picken, Roeland J M Nolte, Eduardo Mendes, and Alan E Rowan. Responsive biomimetic networks from polyisocyanopeptide hydrogels. *Nature*, 493(7434):651–655, January 2013. ISSN 1476-4687. doi: 10.1038/nature11839. URL http://www.ncbi.nlm.nih.gov/pubmed/23354048. (Cited on pages 3, 4, and 5.)

[7] O. Pelletier, E. Pokidysheva, L. S. Hirst, N. Bouxsein, Y. Li, and C. R. Safinya. Structure of Actin Cross-Linked with α-Actinin: A Network of Bundles. *Physical Review Letters*, 91(14):3–6, September 2003. ISSN 0031-9007. doi: 10.1103/PhysRevLett.91.148102. URL http://link.aps.org/doi/10.1103/PhysRevLett.91.148102. (Cited on pages 3 and 4.)

[8] Linda S. Hirst, Roger Pynn, Robijn F. Bruinsma, and Cyrus R. Safinya. Hierarchical self-assembly of actin bundle networks: gels with surface protein skin layers. *The Journal of chemical physics*, 123(10):104902, September 2005. URL http://link.aip.org/link/doi/10.1063/1.1961229/html. (Cited on pages 3, 19, 30, and 32.)

[9] L. Hirst and C. Safinya. Skin Layer at the Actin-Gel Surface: Quenched Protein Membranes form Flat, Crumpled, and Tubular Morphologies. *Physical Review Letters*, 93(1):018101, June 2004. ISSN 0031-9007. doi: 10.1103/PhysRevLett.93.018101. URL http://link.aps.org/doi/10.1103/PhysRevLett.93.018101. (Cited on pages 3, 19, 30, and 32.)

[10] Animesh Agrawal, Nima Rahbar, and Paul D Calvert. Strong fiber-reinforced hydrogel. *Acta biomaterialia*, 9(2):5313–8, February 2013. ISSN 1878-7568. doi: 10.1016/j.actbio.2012.10.011. URL http://www.ncbi.nlm.nih.gov/pubmed/23107796. (Cited on page 3.)

[11] Elsie S Place, Nicholas D Evans, and Molly M Stevens. Complexity in biomaterials for tissue engineering. *Nature materials*, 8(6):457–470, June 2009. ISSN 1476-1122. doi: 10.1038/nmat2441. URL http://www.ncbi.nlm.nih.gov/pubmed/19458646. (Cited on page 3.)

[12] N. A. Peppas, J. Z. Hilt, A. Khademhosseini, and R. Langer. Hydrogels in Biology and Medicine: From Molecular Principles to Bionanotechnology. *Advanced Materials*, 18(11):1345–1360, June 2006. ISSN 0935-9648. doi: 10.1002/adma.200501612. URL http://doi.wiley.com/10.1002/adma.200501612. (Cited on page 3.)

[13] Andrew R Hirst, Beatriu Escuder, Juan F Miravet, and David K Smith. High-tech applications of self-assembling supramolecular nanostructured gel-phase materials: from regenerative medicine to electronic devices. *Angewandte Chemie (International ed. in English)*, 47(42):8002–8018, January 2008. ISSN 1521-3773. doi: 10.1002/anie.200800022. URL http://www.ncbi.nlm.nih.gov/pubmed/18825737.

[14] Joerg C Tiller. Increasing the local concentration of drugs by hydrogel formation. *Angewandte Chemie (International ed. in English)*, 42(27):3072–5, July

2003. ISSN 1433-7851. doi: 10.1002/anie.200301647. URL http://www.ncbi.nlm.nih.gov/pubmed/12866093. (Cited on page 3.)

[15] K M Schmoller, P Fernández, R C Arevalo, D L Blair, and a R Bausch. Cyclic hardening in bundled actin networks. *Nature communications*, 1:134, January 2010. ISSN 2041-1723. doi: 10.1038/ncomms1134. URL http://www.ncbi.nlm.nih.gov/pubmed/21139579. (Cited on pages 3 and 4.)

[16] K M Schmoller, O Lieleg, and a R Bausch. Structural and viscoelastic properties of actin/filamin networks: cross-linked versus bundled networks. *Biophysical journal*, 97(1):83–89, July 2009. ISSN 1542-0086. doi: 10.1016/j.bpj.2009.04.040. URL http://www.pubmedcentral.nih.gov/articlerender.fcgi?artid=2711384&tool=pmcentrez&rendertype=abstract. (Cited on page 4.)

[17] JX X Tang and PA a. Janmey. The polyelectrolyte nature of F-actin and the mechanism of actin bundle formation. *Journal of Biological Chemistry*, 271(15):8556–8563, April 1996. ISSN 00219258. doi: 10.1074/jbc.271.15.8556. URL http://www.jbc.org/cgi/doi/10.1074/jbc.271.15.8556http://www.jbc.org/content/271/15/8556.short.

[18] Lior Haviv, Nir Gov, Yaron Ideses, and Anne Bernheim-Groswasser. Thickness distribution of actin bundles in vitro. *European biophysics journal : EBJ*, 37(4):447–454, April 2008. ISSN 0175-7571. doi: 10.1007/s00249-007-0236-1. URL http://www.ncbi.nlm.nih.gov/pubmed/18004557.

[19] M M a E Claessens, C Semmrich, L Ramos, and a R Bausch. Helical twist controls the thickness of F-actin bundles. *Proceedings of the National Academy of Sciences of the United States of America*, 105(26):8819–22, July 2008. ISSN 1091-6490. doi: 10.1073/pnas.0711149105. URL http://www.pubmedcentral.nih.gov/articlerender.fcgi?artid=2449323&tool=pmcentrez&rendertype=abstract.

[20] J J Otto, R E Kane, and J Bryan. Formation of filopodia in coelomocytes: localization of fascin, a 58,000 dalton actin cross-linking protein. *Cell*, 17(2):285–293, June 1979. ISSN 0092-8674. URL http://www.ncbi.nlm.nih.gov/pubmed/378407.

[21] Thomas E Angelini, Hongjun Liang, Willy Wriggers, and Gerard C L Wong. Like-charge attraction between polyelectrolytes induced by counterion charge density waves. *Proceedings of the National Academy of Sciences of the United States of America*, 100(15):8634–7, July 2003. ISSN 0027-8424. doi: 10.1073/pnas.1533355100. URL

http://www.pubmedcentral.nih.gov/articlerender.fcgi?artid=166363&tool=pmcentrez&rendertype=abstract.

[22] Lam T. Nguyen and Linda S. Hirst. Polymorphism of highly cross-linked F-actin networks: Probing multiple length scales. *Physical Review E*, 83(3):1–9, March 2011. ISSN 1539-3755. doi: 10.1103/PhysRevE.83.031910. URL http://link.aps.org/doi/10.1103/PhysRevE.83.031910. (Cited on page 10.)

[23] Lam T. Nguyen, Wei Yang, Qi Wang, and Linda S. Hirst. Molecular dynamics simulation of F-actin reveals the role of cross-linkers in semi-flexible filament assembly. *Soft Matter*, 5(10):2033, 2009. URL http://xlink.rsc.org/?DOI=b817927a. (Cited on pages 10 and 26.)

[24] R K Meyer and U Aebi. Bundling of actin filaments by alpha-actinin depends on its molecular length. *The Journal of cell biology*, 110(6):2013–2024, June 1990. ISSN 0021-9525. URL http://www.pubmedcentral.nih.gov/articlerender.fcgi?artid=2116144&tool=pmcentrez&rendertype=abstract.

[25] D H Wachsstock, W H Schwartz, and T D Pollard. Affinity of alpha-actinin for actin determines the structure and mechanical properties of actin filament gels. *Biophysical journal*, 65(1):205–214, July 1993. ISSN 0006-3495. doi: 10.1016/S0006-3495(93)81059-2. URL http://www.pubmedcentral.nih.gov/articlerender.fcgi?artid=1225716&tool=pmcentrez&rendertype=abstract.

[26] Y Tseng, E Fedorov, J M McCaffery, S C Almo, and D Wirtz. Micromechanics and ultrastructure of actin filament networks crosslinked by human fascin: a comparison with alpha-actinin. *Journal of molecular biology*, 310(2):351–66, July 2001. ISSN 0022-2836. doi: 10.1006/jmbi.2001.4716. URL http://www.ncbi.nlm.nih.gov/pubmed/11428894.

[27] Oliver Lieleg, Kurt M. Schmoller, Christian J. Cyron, Yuxia Luan, Wolfgang a. Wall, and Andreas R. Bausch. Structural polymorphism in heterogeneous cytoskeletal networks. *Soft Matter*, 5(9):1796, 2009. ISSN 1744-683X. doi: 10.1039/b814555p. URL http://xlink.rsc.org/?DOI=b814555p.

[28] O. Lieleg, M. Claessens, C. Heussinger, E. Frey, and a. Bausch. Mechanics of Bundled Semiflexible Polymer Networks. *Physical Review Letters*, 99(8):088102, August 2007. ISSN 0031-9007. doi: 10.1103/PhysRevLett.99.088102. URL http://link.aps.org/doi/10.1103/PhysRevLett.99.088102.

[29] Itamar Borukhov, Robijn F Bruinsma, William M Gelbart, and Andrea J Liu. Structural polymorphism of the cytoskeleton: a model of linker-assisted filament aggregation. *Proceedings of the National Academy of Sciences of the United*

States of America, 102(10):3673–8, March 2005. ISSN 0027-8424. doi: 10.1073/pnas.0404140102. URL http://www.pubmedcentral.nih.gov/articlerender.fcgi?artid=553289&tool=pmcentrez&rendertype=abstract.

[30] M. Hosek and J. Tang. Polymer-induced bundling of F actin and the depletion force. *Physical Review E*, 69(5):51907, May 2004. ISSN 1539-3755. doi: 10.1103/PhysRevE.69.051907. URL http://link.aps.org/doi/10.1103/PhysRevE.69.051907.

[31] Oliver Lieleg, Mireille M a. E Claessens, and Andreas R Bausch. Structure and dynamics of cross-linked actin networks. *Soft Matter*, 6(2):218, 2010. ISSN 1744-683X. doi: 10.1039/b912163n. URL http://xlink.rsc.org/?DOI=b912163n. (Cited on page 22.)

[32] Pavel Kraikivski, Boris Slepchenko, and Igor Novak. Actin Bundling: Initiation Mechanisms and Kinetics. *Physical Review Letters*, 101(12):128102, September 2008. ISSN 0031-9007. doi: 10.1103/PhysRevLett.101.128102. URL http://link.aps.org/doi/10.1103/PhysRevLett.101.128102.

[33] Daniel J Needleman, Miguel a Ojeda-Lopez, Uri Raviv, Herbert P Miller, Leslie Wilson, and Cyrus R Safinya. Higher-order assembly of microtubules by counterions: from hexagonal bundles to living necklaces. *Proceedings of the National Academy of Sciences of the United States of America*, 101(46):16099–103, November 2004. ISSN 0027-8424. doi: 10.1073/pnas.0406076101. URL http://www.pubmedcentral.nih.gov/articlerender.fcgi?artid=528963&tool=pmcentrez&rendertype=abstract. (Cited on page 3.)

[34] James C Phillips, Rosemary Braun, Wei Wang, James Gumbart, Emad Tajkhorshid, Elizabeth Villa, Christophe Chipot, Robert D Skeel, Laxmikant Kalé, and Klaus Schulten. Scalable molecular dynamics with NAMD. *Journal of computational chemistry*, 26(16):1781–1802, December 2005. ISSN 0192-8651. doi: 10.1002/jcc.20289. URL http://www.pubmedcentral.nih.gov/articlerender.fcgi?artid=2486339&tool=pmcentrez&rendertype=abstract. (Cited on page 7.)

[35] Michael De Podesta. *Understanding the Properties of Matter*. CRC Press, 2002. (Cited on page 17.)

[36] Benoit B Mandelbrot. *The fractal geometry of nature*. Macmillan, 1983. (Cited on page 17.)

[37] Gregory M. Grason and Robijn F. Bruinsma. Chirality and Equilibrium Biopolymer Bundles. *Physical Review Letters*, 99(9):098101, August 2007. ISSN

0031-9007. doi: 10.1103/PhysRevLett.99.098101. URL http://link.aps.org/doi/10.1103/PhysRevLett.99.098101. (Cited on page 26.)

[38] Claus Heussinger and Gregory M Grason. Theory of crosslinked bundles of helical filaments: intrinsic torques in self-limiting biopolymer assemblies. *The Journal of chemical physics*, 135(3):035104, July 2011. ISSN 1089-7690. doi: 10.1063/1.3610431. URL http://arxiv.org/abs/1104.5207. (Cited on page 26.)

[39] P. Prybytak, W. J. Frith, and D. J. Cleaver. Hierarchical self-assembly of chiral fibres from achiral particles. *Interface Focus*, 2(5):651–657, March 2012. ISSN 2042-8898. doi: 10.1098/rsfs.2011.0104. URL http://rsfs.royalsocietypublishing.org/cgi/doi/10.1098/rsfs.2011.0104. (Cited on page 26.)

[40] Yehuda Snir and Randall D Kamien. Entropically driven helix formation. *Science (New York, N.Y.)*, 307(5712):1067, February 2005. ISSN 1095-9203. doi: 10.1126/science.1106243. URL http://www.ncbi.nlm.nih.gov/pubmed/15718461. (Cited on page 26.)

[41] Raghunath Chelakkot and Thomas Gruhn. Length dependence of crosslinker induced network formation of rods: a Monte Carlo study. *Soft Matter*, 8(46):11746, 2012. ISSN 1744-683X. doi: 10.1039/c2sm07379j. URL http://xlink.rsc.org/?DOI=c2sm07379j. (Cited on page 32.)

[42] Ronald J. Pandolfi, Lauren Edwards, David Johnston, Peter Becich, and Linda S. Hirst. Designing Highly Tunable Semiflexible Filament Networks. *Physical Review E*, 89(6):062602, June 2014. ISSN 1539-3755. doi: 10.1103/PhysRevE.89.062602. URL http://link.aps.org/doi/10.1103/PhysRevE.89.062602. (Cited on page 33.)

[43] Ronald J. Pandolfi, Lauren Edwards, and Linda S. Hirst. An Analytic Toolbox for Simulated Filament Networks. *MRS Proceedings*, 1688:mrss14–1688–y05–18, September 2014. ISSN 1946-4274. doi: 10.1557/opl.2014.870. URL http://journals.cambridge.org/abstract_S1946427414008707. (Cited on page 33.)

[44] Shelley A Claridge, A W Castleman, Shiv N Khanna, Christopher B Murray, Ayusman Sen, and Paul S Weiss. Cluster-assembled materials. *ACS nano*, 3(2):244–55, February 2009. ISSN 1936-086X. doi: 10.1021/nn800820e. URL http://dx.doi.org/10.1021/nn800820e. (Cited on page 35.)

[45] Chu-Young Cho, Sang-Jun Lee, Jung-Hoon Song, Sang-Hyun Hong, Song-Mae Lee, Yong-Hoon Cho, and Seong-Ju Park. Enhanced optical output power of green light-emitting diodes by surface plasmon of gold nanoparticles. *Applied Physics Letters*, 98(5):051106, 2011. ISSN 00036951. doi:

10.1063/1.3552968. URL http://scitation.aip.org/content/aip/journal/apl/98/5/10.1063/1.3552968. (Cited on page 35.)

[46] M. Quinten, A. Leitner, J. R. Krenn, and F. R. Aussenegg. Electromagnetic energy transport via linear chains of silver nanoparticles. *Optics Letters*, 23 (17):1331, September 1998. ISSN 0146-9592. doi: 10.1364/OL.23.001331. URL http://ol.osa.org/abstract.cfm?URI=ol-23-17-1331. (Cited on page 35.)

[47] Alexander O. Govorov, Garnett W. Bryant, Wei Zhang, Timur Skeini, Jaebeom Lee, Nicholas A. Kotov, Joseph M. Slocik, and Rajesh R. Naik. Exciton-Plasmon Interaction and Hybrid Excitons in Semiconductor-Metal Nanoparticle Assemblies. *Nano Letters*, 6(5):984–994, May 2006. ISSN 1530-6984. doi: 10.1021/nl0602140. URL http://dx.doi.org/10.1021/nl0602140. (Cited on page 35.)

[48] C. Binns, M. Maher, Q. Pankhurst, D. Kechrakos, and K. Trohidou. Magnetic behavior of nanostructured films assembled from preformed Fe clusters embedded in Ag. *Physical Review B*, 66(18):184413, November 2002. ISSN 0163-1829. doi: 10.1103/PhysRevB.66.184413. URL http://link.aps.org/doi/10.1103/PhysRevB.66.184413. (Cited on page 35.)

[49] S. Crooker, J. Hollingsworth, S. Tretiak, and V. Klimov. Spectrally Resolved Dynamics of Energy Transfer in Quantum-Dot Assemblies: Towards Engineered Energy Flows in Artificial Materials. *Physical Review Letters*, 89(18): 186802, October 2002. ISSN 0031-9007. doi: 10.1103/PhysRevLett.89.186802. URL http://link.aps.org/doi/10.1103/PhysRevLett.89.186802. (Cited on page 35.)

[50] Tae-Ho Kim, Kyung-Sang Cho, Eun Kyung Lee, Sang Jin Lee, Jungseok Chae, Jung Woo Kim, Do Hwan Kim, Jang-Yeon Kwon, Gehan Amaratunga, Sang Yoon Lee, Byoung Lyong Choi, Young Kuk, Jong Min Kim, and Kinam Kim. Full-colour quantum dot displays fabricated by transfer printing. *Nature Photonics*, 5(3):176–182, February 2011. ISSN 1749-4885. doi: 10.1038/nphoton.2011.12. URL http://dx.doi.org/10.1038/nphoton.2011.12. (Cited on page 35.)

[51] W H Goldmann, M Tempel, I Sprenger, G Isenberg, and R M Ezzell. Viscoelasticity of actin-gelsolin networks in the presence of filamin. *European journal of biochemistry / FEBS*, 246(2):373–379, June 1997. ISSN 0014-2956. URL http://www.ncbi.nlm.nih.gov/pubmed/9208927. (Cited on page 35.)

[52] X Michalet, F F Pinaud, L A Bentolila, J M Tsay, S Doose, J J Li, G Sundaresan, A M Wu, S S Gambhir, and S Weiss. Quantum dots for live cells, in vivo imaging, and diagnostics. *Science (New York, N.Y.)*,

307(5709):538–44, January 2005. ISSN 1095-9203. doi: 10.1126/science.1104274. URL http://www.pubmedcentral.nih.gov/articlerender.fcgi?artid=1201471&tool=pmcentrez&rendertype=abstract. (Cited on page 35.)

[53] Tomasz Dietl. A ten-year perspective on dilute magnetic semiconductors and oxides. *Nature materials*, 9(12):965–74, December 2010. ISSN 1476-1122. doi: 10.1038/nmat2898. URL http://dx.doi.org/10.1038/nmat2898. (Cited on page 35.)

[54] Numpon Insin, Joseph B Tracy, Hakho Lee, John P Zimmer, Robert M Westervelt, and Moungi G Bawendi. Incorporation of iron oxide nanoparticles and quantum dots into silica microspheres. *ACS nano*, 2(2):197–202, February 2008. ISSN 1936-086X. doi: 10.1021/nn700344x. URL http://dx.doi.org/10.1021/nn700344x. (Cited on page 35.)

[55] Susan P Foy, Rachel L Manthe, Steven T Foy, Sanja Dimitrijevic, Nishanth Krishnamurthy, and Vinod Labhasetwar. Optical imaging and magnetic field targeting of magnetic nanoparticles in tumors. *ACS nano*, 4(9):5217–24, September 2010. ISSN 1936-086X. doi: 10.1021/nn101427t. URL http://www.pubmedcentral.nih.gov/articlerender.fcgi?artid=2947615&tool=pmcentrez&rendertype=abstract. (Cited on page 35.)

[56] B. Kardynal. Introduction to the Physics of Quantum Dots. *Acta Physica Polonica A*, 100(3):275–286, 2001. URL http://yadda.icm.edu.pl/yadda/element/bwmeta1.element.bwnjournal-article-appv100n319kz. (Cited on page 37.)

[57] Maksym F Prodanov, Nataliya V Pogorelova, Alexander P Kryshtal, Andrey S Klymchenko, Yves Mely, Vladimir P Semynozhenko, Alexander I Krivoshey, Yurii A Reznikov, Sergey N Yarmolenko, John W Goodby, and Valerii V Vashchenko. Thermodynamically stable dispersions of quantum dots in a nematic liquid crystal. *Langmuir : the ACS journal of surfaces and colloids*, 29(30):9301–9, July 2013. ISSN 1520-5827. doi: 10.1021/la401475b. URL http://dx.doi.org/10.1021/la401475b. (Cited on page 41.)

[58] Andrea L. Rodarte, Fredy Cisneros, Linda S. Hirst, and Sayantani Ghosh. Dye-integrated cholesteric photonic luminescent solar concentrator. *Liquid Crystals*, 41(10):1442–1447, May 2014. ISSN 0267-8292. doi: 10.1080/02678292.2014.924163. URL http://dx.doi.org/10.1080/02678292.2014.924163. (Cited on page 56.)